Impacts of tidal mixing on diurnal and intraseasonal air-sea interactions in the Maritime Continent

John Steffen [a,c,*], Hyodae Seo [a], Carol Anne Clayson [a], Suyang Pei [b], Toshiaki Shinoda [b]

[a] *Woods Hole Oceanographic Institution, USA*
[b] *Texas A&M University – Corpus Christi, USA*
[c] *Science Applications International Corporation, USA*

ARTICLE INFO

Handling editor. Prof. J Aristegui

ABSTRACT

The Maritime Continent (MC) is a region with enhanced tidal mixing and ocean cooling, which influences regional-scale sea surface temperatures (SSTs). We examine the coupled impacts of tidal mixing on near-surface stratification, SST, and deep convection on diurnal and intraseasonal time-scales, using ensembles of high-resolution, coupled ocean-atmosphere regional model simulations, with and without tidal forcing. Results show that the area-averaged SST in the eastern MC is reduced by 0.20 °C due to tidal forcing, with cooling exceeding 1 °C in the nearshore zones of shallow and complex bathymetry. The reduced SSTs decrease surface heat fluxes, leading to tropospheric drying and reduced precipitation, which are most pronounced in the near-shore zones. The results show that the magnitude of tidally-induced SST cooling is phase-dependent during the passage of the Madden Julian Oscillation (MJO). Strong westerly winds enhance entrainment cooling through wind-driven mixing and upwelling during the active phase. Conversely, the upper-ocean stratification is enhanced during the suppressed phase, and SSTs are less sensitive to subsurface cooling. Such spatio-temporal variability in the SST response to tides is accompanied by consistent changes to deep convection and atmospheric circulation. On the diurnal time-scale, nearshore cooling weakens the early-morning convection when the land-based convection propagates offshore and interacts with the cooler SST. On intraseasonal time-scales, the coupling between SST and precipitation is strengthened because of the asymmetric impacts of tide-induced mixing on SST and MJO-induced winds. The robust SST and precipitation responses demonstrated in this study suggest the need for an accurate representation of tidal forcing and vertical mixing processes in local MJO prediction models for the MC.

1. Introduction

The Maritime Continent (MC) is a region with enhanced vertical mixing in the upper ocean induced by tides, which manifests most strongly as subsurface cooling localized near sills, channels, and seamounts (e.g., Ffield and Gordon, 1992, 1996; Koch-Larrouy et al., 2007; Robertson and Ffield, 2005, 2008; Susanto et al., 2000; Gordon and Coauthors, 2010). The observations show vertical mixing primarily over shallow and complex bathymetric features (e.g., Hatayama, 2004), while the marginal seas in the interior MC feature relatively weak tidal mixing but complex reflection and refraction patterns of tidally-generated internal waves (e.g., Alford et al., 1999; Ray et al. 2005; Nagai and Hibiya, 2015; Koch-Larrouy et al., 2015). The wind-driven mixing during intense wind events reinforces the

tide-induced mixing, entraining subsurface water into the mixed layer and cooling the SST. The wind-driven circulation, such as coastal upwelling and Ekman transport, can increase the spatial coverage of localized tidal mixing effects on SST into the interior of marginal seas (Kida and Wijffels, 2012; Nagai and Hibiya, 2020; Pei et al., 2021). Balancing the lateral advection from the western Pacific via the Indonesian Throughflow (ITF), the tidal mixing effect on SST plays a critical role in maintaining the basic stratification of the upper ocean in the MC (Koch-Larrouy et al., 2007; Ray and Susanto, 2016).

The effects of tidal mixing on SST in the MC have been documented in previous studies based on satellite observations (Ffield and Gordon, 1996; Ray and Susanto, 2016), in situ microstructure measurements (Alford et al., 1999), and numerical models with explicit or implicit tidal forcing (e.g., Schiller, 2004; Jochum and Potemra, 2008; Nagai and

---

Hibiya, 2015; Nagai and Bouruet-Aubertot, 2017; Nugroho et al., 2018). These studies suggest a wide range of basin-wide SST cooling of 0.1–1.0 °C in various parts of the MC region. Based on a bulk flux calculation, a 0.5 °C cooling of SST is equivalent to about 20 W m^{-2} decrease in latent heat flux using mean meteorological and ocean variables in this region (Ffield and Gordon, 1996). Therefore, tidally-driven SST cooling has considerable amplitude in comparison to the intraseasonal standard deviation of SST and net surface heat flux in the MC, which is about 0.4 °C and 40 W m^{-2}, respectively (Vialard et al., 2013).

Whether tidally-induced SST cooling modulates the regional convection and circulation is an important question, given that the MC is an integral part of the global climate system, supporting one of the most vigorous convective regions observed in the world oceans (Yoneyama and Zhang, 2020). The abundant latent heat release over warm SSTs in the MC (Ramage, 1968) shapes regional climate and influences high-latitude weather patterns through teleconnections (Jin and Hoskins, 1995; McBride et al., 2003; Neale and Slingo, 2003; Adames and Wallace, 2014; Sprintall et al., 2014). This study tests the hypothesis that the enhanced vertical mixing by tides in the MC plays a critical role in setting the upper ocean stratification and SST on diurnal and intraseasonal time-scales, inducing consistent changes in regional atmospheric circulation.

This study seeks to identify the responses in atmospheric circulation and convection mainly on two time-scales: diurnal and intraseasonal. On the diurnal time-scale, deep convection is particularly strong in the MC as daytime heating over the larger islands results in a late-afternoon and early-evening peak in convection over land (Qian, 2008). The land-based convection subsequently propagates offshore during the early-morning hours, often developing into mesoscale convective systems accompanied by major rain events (e.g., Mori and Coauthors, 2004; Fujita et al., 2011; Ichikawa and Yasunari, 2006; Wang and Sobel, 2017; Coppin and Bellon, 2019a, b). Complex time-scale interactions between the diurnal cycle of convection and the Madden-Julian Oscillation (MJO) have been demonstrated to modulate local MJO propagation near or through the MC (Peatman et al., 2014; Hagos et al., 2016; Vincent and Lane, 2016; Sakaeda et al., 2017; Tan et al., 2021, 2022), which contributes to the barrier effect (Ling et al., 2019). For example, diurnal convection triggers land-based precipitation, which competes with and limits precipitation over the ocean during MJO passage (Sobel et al., 2010; Zhang and Ling, 2017). What aspects of the diurnal convection characteristics are sensitive to the tide-induced SST in the MC?

On an intraseasonal time-scale, the variability in regional convection and circulation is dominated by the MJO during boreal winter, characterized by coupled air-sea interactions leading to large-scale, zonally-oriented atmospheric overturning circulation and precipitation anomalies on a 40-50-day period (Madden and Julian, 1971, 1994). Of the MJO events originating from the Indian Ocean, only about half propagate across the MC into the Western Pacific. During this period, most of the MJOs become considerably weakened (Zhang and Ling, 2017), a phenomenon named the "barrier effect". Various processes, including a strong diurnal cycle in land-based convection and multi-scale air-sea interaction complicated by elevated terrains and land-sea geometry, have been implicated as critical factors for the observed changes in MJO patterns across the MC (Zhang and Ling, 2017; Kim et al., 2018). However, the current discussion in the literature omits the possible role of tides. How does the tidally-induced SST cooling modulate the intraseasonal MJO-ocean interaction and intraseasonal rainfall variability in the MC?

Complex bathymetry and coastal geometry in the MC create substantial spatial variability in tidal mixing, which affects upper-ocean stratification and SST and, thus, their influence on the atmosphere. Global climate models (GCMs) struggle with systematic biases in the mean state representation of moisture and precipitation over the MC region, limiting model prediction skills (Kim et al., 2018; Wang et al., 2019). For example, the diurnal cycle of convection over MC islands is poorly resolved (Love et al., 2011), the MJO barrier effect is overstated

(e.g., Inness and Slingo, 2003; Kim and Coauthors, 2009), and a persistent dry bias exists over the MC (Schiemann et al., 2014), which altogether influence the MJO propagation (Raymond, 2001; Sobel and Maloney, 2012; Adames and Kim, 2016; Zhang et al., 2020). The adoption of coupled regional modeling within the MC has ameliorated some of the issues inherent to GCMs and improved precipitation characteristics throughout the region (Aldrian et al., 2005). Recent studies implementing high-resolution regional models with explicit convection (Argüeso et al., 2020), or convection-permitting, resolutions have improved MC precipitation, particularly at the diurnal time scale (Wei et al., 2020).

To mitigate the resolution limitation in representing the enhanced spatial variability in the ocean and atmospheric responses to ocean tides, this study uses a regional ocean-atmosphere coupled model, with grid resolutions sufficient to permit deep convection in the atmosphere and resolve fine-scale coastal and nearshore processes in the ocean. Although high-resolution regional atmospheric models, in particular at convection-permitting scales, are known to produce a high precipitation bias over land and steep topography (Vincent and Lane, 2016, 2017), such models nonetheless still improve the overall distribution of precipitation compared to models with parameterized convection (Peatman et al. 2015). Furthermore, high-resolution ocean models and refined physics for vertical mixing and air-sea fluxes are critical to improving the prediction skills of diurnal to intraseasonal SST variation associated with the MJO (e.g., Seo et al., 2014; Ge et al., 2017; Shinoda et al., 2021).

By capturing the direct ocean-atmosphere coupling at a convection-permitting scale and fine ocean scales, this study explores the sensitivity of coupled air-sea processes to tide-induced SST cooling. Our results indicate that robust rainfall responses on diurnal and intraseasonal time-scales are induced by the spatial variability of the upper ocean stratification and SST response to tidal mixing. Since the tidal mixing effect is entirely of oceanic origin, and it is unrelated to the diurnal cycle of thermally-forced convection or the MJO, such robust SST and precipitation responses suggest the need for an accurate representation of tidal forcing and associated vertical mixing processes in prediction models.

The paper is organized in the following way. Section 2 provides details about the regional coupled model and the experiment design. In Section 3, the simulated tides are validated with tide gauge measurements, and the upper ocean mixing and SST responses to tidal forcing are characterized. Section 4 probes the physical processes by which the tide-induced SST cooling influences the time-mean and intraseasonal to diurnal variability in surface meteorology, tropospheric moisture, and regional precipitation. Finally, conclusions about the impact of tidal mixing on both the oceanic and atmospheric responses in the MC are discussed in Section 5.

2. The regional modeland experiment design

2.1. Regional ocean-atmosphere coupled model

In this study, the Scripps Coupled Ocean-Atmosphere Regional (SCOAR) model is utilized (Seo et al., 2007b; 2014), which couples the Weather Research and Forecasting (WRF) model (Skamarock et al., 2008) in the atmosphere to the Regional Ocean Modeling System (ROMS; Haidvogel et al., 2000; Shchepetkin and McWilliams, 2005) in the ocean. The WRF and ROMS models are coupled through the bulk aerodynamic flux formula implemented in ROMS (Fairall et al., 1996, 2003). The ocean current fields are included in the bulk formula to estimate the wind stress based on the relative wind (Seo et al., 2016, 2019; Seo, 2017). The latest information about the coupled model and coupling design can be found in Seo et al. (2021) and Sauvage et al. (2023).

The model domain covers the MC region, excluding New Guinea, spanning 11°S to 11°N and 94.6°E to 135.6°E on a horizontal grid spacing of ~4 km (Fig. 1). The high-resolution 4 km shared grid is
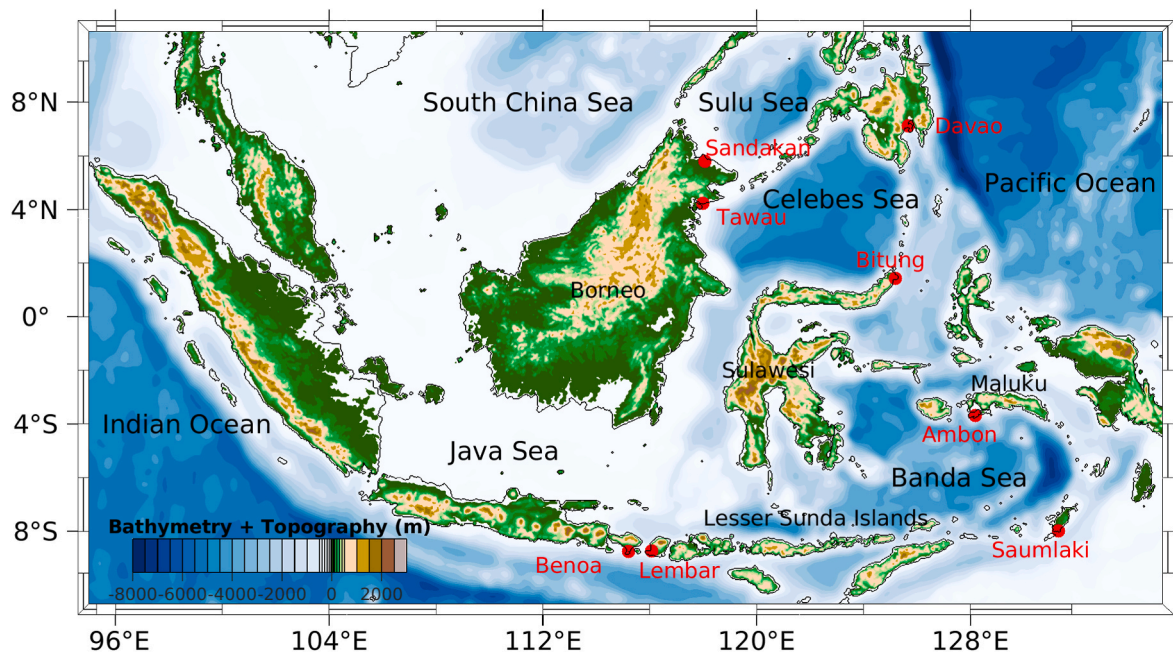
Fig. 1. The SCOAR model domain with representative bathymetry and topography of the coupled model. The locations of the University of Hawaii Sea Level Center (UHSLC) tide gauges (red) and other geographically relevant areas (black) are shown.

convection-permitting in the atmosphere, and it is designed to better resolve the coastal and tidally-driven oceanic processes near complex coastlines and bathymetry of the MC region. The zonal extent of the regional model domain is proportioned to capture sufficient upstream direction, which allows the modeled MJO to respond to tidally-forced SSTs. The southern boundary is confined to 11°S, which does not cover the internal tide sources from the entire Timor and Arafura Seas. A strong tidal mixing response is still simulated along the Lesser Sunda Islands and south Banda Sea regions. Additionally, ROMS is run with a stretched vertical grid with 30 vertical levels and 10 levels within the upper 10 m of the open ocean. The vertical grid in WRF has 35 vertical levels, which is a relatively coarse vertical resolution, but it can still adequately depict localized MJO convection and propagation through the MC. Since the atmosphere and ocean models adopt identical grids with matching land-sea masks, no re-gridding procedure is required in the flux coupler, and the atmosphere can directly interact with the fine-scale coastal ocean variability induced by tides. This has relatively important implications for nearshore diurnal precipitation responses to SST cooling that are coastally enhanced (Section 4.2). These models are coupled at a 1-h frequency to resolve the diurnal warm layer at the ocean surface (Li et al., 2020) and its impacts on diurnal convection in the atmosphere (de Szoeke et al., 2021).

The SCOAR model is run with a suite of atmospheric and oceanographic parameterizations. For shortwave and longwave radiation, the Rapid Radiation Transfer Model (RRTM; Mlawer et al., 1997) and the Goddard scheme (Chou and Suarez, 1999) calculate the radiative transfer through the atmosphere. Land surface processes are modeled using the Noah land surface model (Chen and Dudhia, 2001). The surface layer scheme uses an improved WRF surface layer formulation based on the fifth-generation Pennsylvania State University – National Center for Atmospheric Research Mesoscale Model (MM5) parameterization (Grell et al., 1994; Jiménez et al., 2012). The Yonsei University PBL scheme (YSU; Hong et al., 2006) estimates turbulent fluxes using a first-order scheme. Finally, the WRF single-moment 6-class microphysics package (Hong et al., 2006) is used to classify hydrometeor types. For ROMS, the Mellor-Yamada 2.5 (MY2.5) turbulence closure scheme (Mellor and Yamada, 1982), along with the equilibrium stability function of Kantha and Clayson (1994), determines vertical eddy viscosity and diffusivity. A background vertical mixing coefficient of 10^{-5}

$m^2\,s^{-1}$ is set in both the TIDES and NOTIDES experiments. The 3rd-order upstream biased advection scheme introduces implicit numerical diffusivity (Haidvogel et al., 2000).

ROMS initial and boundary conditions are constructed using the daily Hybrid Coordinate Ocean Model (HYCOM) ocean reanalysis (Metzger and Coauthors, 2014). WRF is initialized and boundary conditions are derived from the 6-hourly Interim European Centre for Medium-Range Weather Forecasts (ECMWF) Reanalysis (ERA-Interim; Dee and Coauthors, 2011), beginning at 0000Z 01 October 2011. ERA-Interim has been widely used for process studies during the Cooperative Indian Ocean experiment on Intraseasonal Variability (CINDY) and the Dynamics of the Madden-Julian Oscillation (DYNAMO) field campaigns of the 2011–2012 fall/winter and it is shown to have high-quality atmospheric data assimilation of upper-air soundings (Ciesielski and Coauthors, 2014). Potential errors are introduced due to resolution jump from ERA-Interim down to the high resolution regional domain. To elicit a better representation of the three MJO events (e.g., Hagos et al., 2011), atmospheric winds above 850 hPa with zonal wavenumbers k=1–3 and meridional wavenumbers l=1–2 ($O(10,000$ km)) are spectrally nudged toward ERA-Interim Reanalysis, which shows distinct MJO propagation in 850 hPa zonal winds (Seo et al., 2014). Therefore, the large-scale atmospheric environment is dynamically constrained, yet the lower tropospheric and near-surface processes are relatively free to respond to the atmospheric and oceanographic forcing. However, despite the large-scale nudging, the tidal rectification effect on SST leaves noticeable imprints in the troposphere during the MJO deep convection, which is discussed further in Section 4.

2.2. Tides experiment design

A set of twin coupled model simulations is conducted, with and without tidal forcing in the ocean component of the coupled model. First, a control simulation is performed using tidal forcing (hereafter referred to as TIDES) from the Oregon State University (OSU) Tidal Prediction Software (OTPS; Egbert and Erofeeva, 2002). Tidal forcing is applied as a 2-D open boundary condition by prescribing the tidal period, elevation amplitude, current phase angle, current inclination angle, and the minimum and maximum tidal current, ellipse semi-minor axes for 13 major tidal constituents: the semi-diurnal tides with ~12 h

periods (M2, S2, N2, K2) and ~6 h periods (M4, Ms4, Mn4), diurnal tides with ~24–27 h periods (K1, O1, P1, Q1) and the lunar fortnightly (Mf) and monthly (Mm) tides. The sensitivity simulation run without tidal forcing (hereafter referred to as NOTIDES) does not apply the tidal forcing to ROMS, but is otherwise identical to TIDES.

The TIDES and NOTIDES experiments are integrated for the three months of October–December 2011, which coincides with the CINDY/DYNAMO field campaign and the three MJO events that propagated toward the MC region (Gottschalck et al., 2013; Li et al., 2015; Wang et al., 2015). The two experiments are designed as a case study to understand the air-sea interactions related to tides during the CINDY/-DYNAMO period. Therefore, the model integration period is short, yet we are able to leverage model ensembles for robustness. Each simulation is repeated three times with slightly perturbed initial atmospheric conditions by adding normally distributed random noise to the temperature fields. The resulting ensemble spread in SST is negligibly small, which shows that the SSTs in each experiment are not overly sensitive to the prescribed atmospheric temperature perturbations. The ensemble-averaged differences between TIDES and NOTIDES represent the rectified effects of tidal forcing only. The ensemble difference is calculated from each pair of runs sharing identical initial conditions, such that there is no influence from the initial condition on the response. Though the model domain covers a large portion of the MC region, and since the tidal effect is concentrated in the eastern MC, unless otherwise noted, the subsequent analysis will focus mainly on the eastern half of the domain. All of the following analyses are based on ensemble averages and statistical significance tests are performed using two-sample *t*-tests of the full set of ensemble members.

2.3. Observational datasets

The following observational datasets are used for analysis and evaluation. First, the tidal heights are analyzed using the tide gauge measurements compiled by the University of Hawaii Sea Level Center (UHSLC; Caldwell et al., 2015). The study also analyzes the two satellite-derived rainfall estimates based on the Tropical Rainfall Measuring Mission (TRMM) 3B42 v7 (TRMM, 2011) and the CPC Morphing Technique (CMORPH) global precipitation estimates v1 (Xie et al., 2019). The SST datasets are obtained from the two satellite-based products: the NOAA Optimally-Interpolated (OI) ¼° daily SST (AVHRR-only, Reynolds et al., 2007) and the 3-hourly ¼° SeaFlux CDR v02 SST (Clayson and Brown, 2016), hereafter referred to as OISST and SFSST, respectively. It should be noted that OISST acts as a foundation SST devoid of diurnal variability, while the SFSST applies a model-based, diurnal warming correction to the OISST. Specifically, SeaFlux implements a regression-based parametrization that fits a daytime heating curve based on variables such as peak solar radiation, daily-averaged wind speed, daily precipitation, and radiative fluxes (Clayson and Brown, 2016; Clayson and Bogdanoff, 2013). Because the diurnal warming is represented in SFSST but not in OISST, and given that the diurnal cycle amplitude of SST is known to raise daily-mean SSTs by several tenths of a degree in the MC (Shinoda and Hendon, 1998; Shinoda, 2005), the time-mean SST from SFSST is expected to be higher than that from OISST in the MC.

3. Ocean responses to tides

3.1. Simulated tides

The simulated tidal elevation characteristics in TIDES are compared to tide gauge measurements. There are eight locations within the eastern MC region with hourly sea level observations during the 3-month study period (Table 1; Fig. 1). The closest ocean grid point is selected for comparison. On average, the nearest ocean grid point is only 4.94 km from the tide gauge location. However, due to the smooth nature of near-coast bathymetry and unresolved coastline features within ROMS,

Table 1
List of UH SLC tide gauge locations in the eastern MC region.

UH #	Version	Location	Country	Latitude/ Longitude	Period of Record
033	a	Bitung	Indonesia	1.440/ 125.193	1986-12-15 to 2018-12-31
133	b	Ambon	Indonesia	−3.683/ 128.183	2008-10-02 to 2018-12-31
163	b	Benoa	Indonesia	−8.745/ 115.210	2006-01-25 to 2018-12-31
420	a	Saumlaki	Indonesia	−7.982/ 131.290	2008-10-02 to 2018-12-31
419	a	Lembar	Indonesia	−8.732/ 116.072	2008-09-23 to 2018-12-24
372	b	Davao	Philippines	7.122/ 125.663	1998-01-01 to 2018-12-31
389	a	Sandakan	Malaysia	5.810/ 118.067	1993-12-25 to 2015-12-31
385	a	Tawau	Malaysia	4.233/ 117.993	1987-06-27 to 2015-02-23

we expect some discrepancy between the simulated and the observed tidal elevations.

First, a Welch's power spectral density (PSD) estimate of sea level is performed for both the TIDES model output and the UHSLC tidal gauge observations at all 8 locations within the eastern MC. Both the model and tide gauge observations have hourly temporal resolution over the three months from 01 October through 31 December 2011. Welch's technique to reduce the variance in PSD estimation is to break the time series into overlapping segments (Hayes 1996; Stoica and Moses, 2005). The PSD is calculated for each segment and then averaged to estimate the true PSD of the full sea level time series. The PSD is estimated using 8 equal-length segments with 50% overlap. This results in a window length of 490 h, or ~20.4 days, sufficient to resolve the diurnal to semi-diurnal tidal signals of interest. The 8-station average of the PSD estimate from observations and collocated model points is compared to a red noise signal (Fig. 2a).

The TIDES ensemble and gauge observations have statistically significant peaks within the PSD at semi-diurnal and diurnal periods (Fig. 2a). The close match between PSD estimates of sea level from TIDES and the tidal gauge measurements indicates that the model realistically simulates the observed tidal periods. Furthermore, a magnitude-squared coherence (Kay, 1988) of sea level is computed between TIDES and the tidal gauge observations using the same segment length and overlap from Welch's PSD estimate (Fig. 2b), where $P_{xx}(f)$ and $P_{yy}(f)$ correspond to the PSDs from the tide gauges and model data, respectively, and $P_{xy}(f)$ is the cross PSD between the two datasets

$$C_{xy}(f) = \frac{|P_{xy}(f)|^2}{P_{xx}(f)P_{yy}(f)}$$

The magnitude-squared coherence ranges between 0 and 1 and higher values, approaching one, indicate strong correspondence between the ROMS model sea level data and the tidal gauge observations. Magnitude-squared coherence values surpass 0.8 at tidal periods near 12 h (M2, S2, N2, and K2) and 24–27 h (K1, O1, P1, and Q1). These analyses demonstrate that the tidal periods and the tidal signature in the sea level are correctly modeled and provide a reasonable estimate of the semi-diurnal and diurnal tides within the eastern MC region.

Furthermore, it is necessary to quantify the tidal mixing intensity across the eastern MC by estimating the modeled vertical diffusivity. First, offline calculations of the gradient Richardson number are performed at locations with strong tidal cooling signatures at or below the ocean mixed layer. The interior mixing of the water column is attributable to marginal instability from shear and internal wave breaking of Kelvin-Helmholtz waves when the critical value of the gradient Richardson number is reached, which is estimated to be near 0.25 (Kunze et al., 1990). Hourly-averaged ROMS model output of
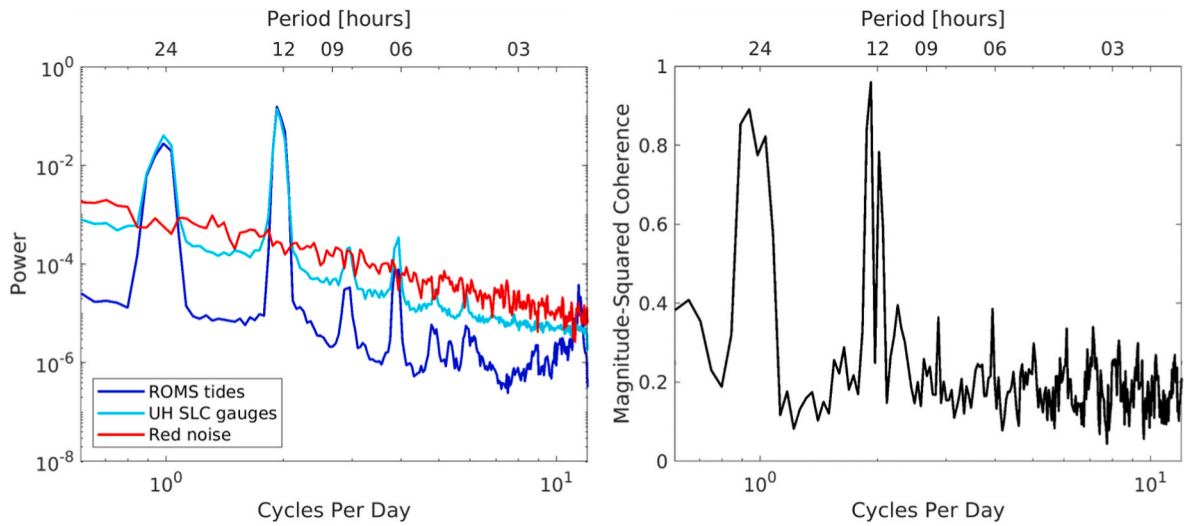
Fig. 2. (a) Log-log plot of the power spectral density (PSD, $m^2\,Hz^{-1}$) estimate of sea level as a function of cycles per day (bottom x-axis) and period (hours, top x-axis) from TIDES (blue) and the 8-member average of UHSLC stations (cyan) compared to a red noise spectrum (red). (b) Semi-log plot of magnitude-squared coherence between sea level from TIDES and an 8-member average of UHSLC stations.

3-dimensional fields of ocean currents and potential density for the one-week November 21–28, corresponding to the active MJO2, are used for these calculations. Due to the hourly-averaged model output and thicker vertical grid layers at depths below the mixed layer, the estimates of gradient Richardson number, and the downstream calculations for TKE dissipation and vertical diffusivity are conservative estimates. As expected, the spatial distribution of marginally unstable gradient Richardson numbers (Fig. 3a) is well-aligned with tidal cooling signatures.

The estimation of the TKE dissipation rate is retrievable for a marginal instability state ($Ri \leq 0.25$) following the equation provided in Section 5 of Wenegrat and McPhaden (2015). Then, the vertical diffusivity (K_v) is derived from Osborn's relationship (Osborn, 1980). Areas of enhanced mixing, where the critical value of Ri is reached, have an area-averaged K_v of 4.9×10^{-2} (Fig. 3b). The maximum vertical diffusivity values of order $10^{-2}\ m^2\ s^{-1}$ are consistent with the previous studies. Outside of these mixing "hot spots" the vertical diffusivity is much lower and largely set by the constant background diffusivity in the model. Since our K_v estimate is spatially limited to areas which are marginally unstable, the spatial pattern of K_v differs from that found in Koch-Larrouy et al. (2007) and Nagai and Hibiya (2015). Since the

offline estimates for Ri and K_v are calculated using hourly-averaged output of temperature, salinity, and current velocity from the ocean model, and due to the relatively coarse temporal model output, these estimates are considerably smaller than instantaneous values computed internally within the model. Also, these estimates are generally smaller than direct microstructure measurements of turbulent dissipation for the same reasons, particularly in the narrow straits of the MC (Koch-Larrouy et al., 2015; Nagai et al., 2021).

3.2. Time-mean SST response

SSTs from TIDES have an area average across the eastern MC of 29.38 °C during the three-month period of study. The average SST in TIDES is comparable to two satellite-derived SST estimates based on the OISST and SFSST, with average SSTs of 29.30 °C and 29.50 °C, respectively (Fig. 4). The modeled SST and SFSST are mostly warmer than the OISST, primarily because of their ability to represent the diurnal cycle amplitude of SST. The inclusion of both observational SST products provides a range of values for comparison, bounded on the bottom by OISST and the top by SFSST (Fig. 3a). In regions where the coupled model is much warmer than observations, the inclusion of tidal forcing
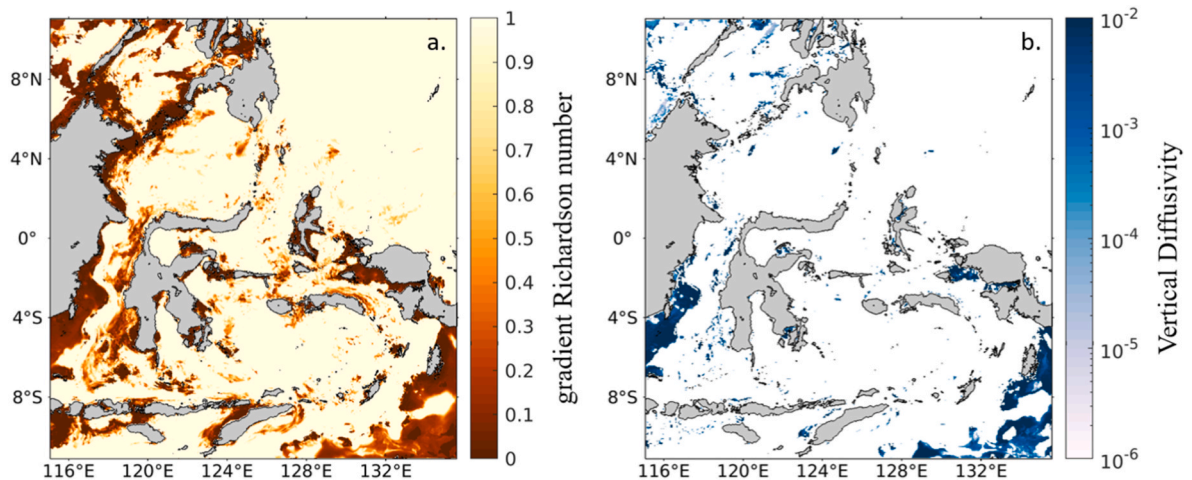

Fig. 3. Spatial distribution of model-derived values of (a.) gradient Richardson number [dimensionless ratio] and (b.) vertical diffusivity [$m^2\ s^{-1}$] from the TIDES experiment.

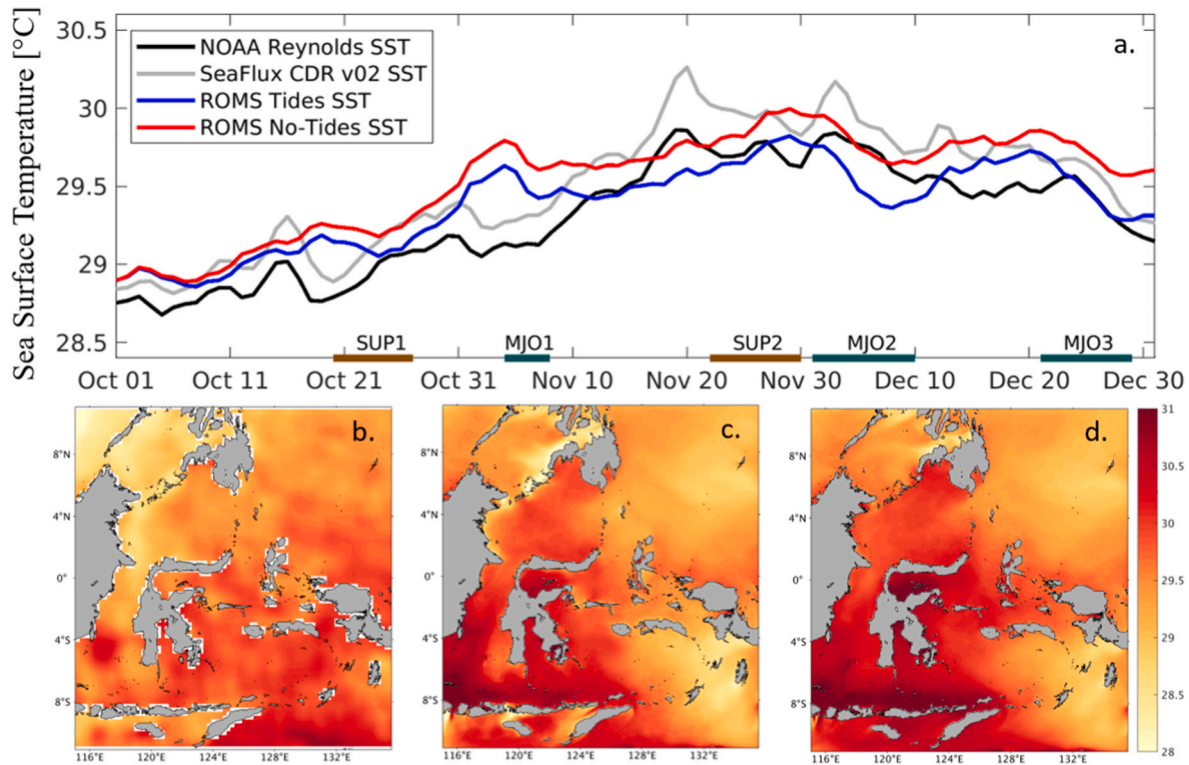**Fig. 4.** (a) Time series of daily SST (°C) averaged over the eastern MC from the model simulations compared with two satellite-derived SST products from October through December 2011. Suppressed (brown) and active (green) phases of MJO within the MC are indicated along the x-axis (top panel). (Lower panels) Two-month averaged SSTs (Nov.–Dec. 2011) from (b) NOAA OISST, (c) TIDES ensemble, and (d) NOTIDES ensemble.

in TIDES counteracts the SST warming and is more aligned with observations.

In the time-mean, the tidal rectification of SSTs (TIDES-NOTIDES) results in an area-averaged SST cooling of 0.20 °C (Fig. 4). The SST response of this magnitude is nontrivial in the perspective of intra-seasonal air-sea interaction, considering that the typical SST anomaly associated with the MJO in the MC is known to be ~0.4 °C (Vialard et al., 2013). Hence, the reduced time-mean SST is expected to be accompanied by a consistent reduction in the time-mean atmospheric convective activity (Section 4.1). The spatial pattern of tide-induced SST cooling reveals substantial spatial variability. Fig. 4a indicates highly localized tidal mixing sites, where the SST cooling exceeds 1 °C. The enhanced cooling is concentrated in the nearshore and coastal zones of the MC islands near the Lesser Sunda Islands, Sulawesi, the Banda Arc, and the Sulu Sill. In contrast, the SST cooling signature in the interior regions is comparatively less pronounced, where advection, Ekman transport, and other ocean processes can expand the spatial coverage of the reduced SSTs (Nagai and Hibiya, 2020; Pei et al., 2021).

3.3. Diurnal cycle amplitude of SST

The average diurnal warming within the eastern MC estimated from SFSST is 0.45 °C, as measured by the peak-to-trough difference in the averaged diurnal composites, while the diurnal cycle amplitude of SST warming in the TIDES ensemble is 0.70 °C (Fig. 6). The larger diurnal cycle amplitude of SST in the model compared to SFSST could partly result from higher temporal and spatial resolution than SFSST, as shallow, protected areas near the coast are likely to experience more robust diurnal warming. In contrast, coastal regions are more uncertain in the SFSST, partly due to the 1° by 1° resolution shortwave radiation product used.

By including tidal forcing in the ocean, the magnitude of the diurnal warming increases slightly by 0.09 °C compared to the NOTIDES

ensemble, which has an average diurnal warming of 0.61 °C. The areas with the most distinguishable differences in diurnal warming of SST between the TIDES and NOTIDES ensembles (Fig. 6c) are characterized by strong tidal cooling signatures (Fig. 5). The increased diurnal warming in TIDES is likely an indirect response to modulated surface fluxes and near-surface meteorology due to tidal cooling (e.g., Clayson and Bogdanoff, 2013). Indeed, the TIDES ensemble shows higher incoming solar radiation (Fig. 7d and e) and weaker near-surface wind speeds (Fig. 7f) than the NOTIDES ensemble, which would favor the amplified diurnal warming of SST. Such changes in solar radiation and wind speed reflect aspects of indirect atmospheric circulation and convection responses to the SST cooling, which is discussed further in Section 4. The coast-enhanced SST cooling by TIDES will likely influence the diurnal convective systems in the coastal oceans (Section 4.2).

3.4. Intraseasonal SST response

The time-series of SST cooling in different sub-regions of the eastern MC is shown in Fig. 5b. The first month of model integration is the ocean model spin-up time, after which the area-averaged SST cooling in the eastern MC has stabilized (Fig. 5). The time evolution of SST cooling shows that the magnitude of tide-induced SST cooling is not constant in time but instead exhibits discernible intraseasonal variability that may be related to the MJO active-inactive cycles. For example, during active phases of MJO2 (phases 4–5 in the MC as defined by the Wheeler-Hendon index, Wheeler and Hendon, 2004), SST differences are more enhanced (−0.51 °C) compared to the suppressed phases (phases 2–3) (−0.27 °C) in the Banda arc region. This indicates a possible mechanism linking tidal forcing, SSTs, and the MJO on intraseasonal time-scales, analogous to the seasonal impact of tides on SST modulated by the monsoons (Kida and Wijffels, 2012).

The apparent MJO-phase-dependent SST cooling effect by tides is due to subsurface cooling maxima, which induces enhanced
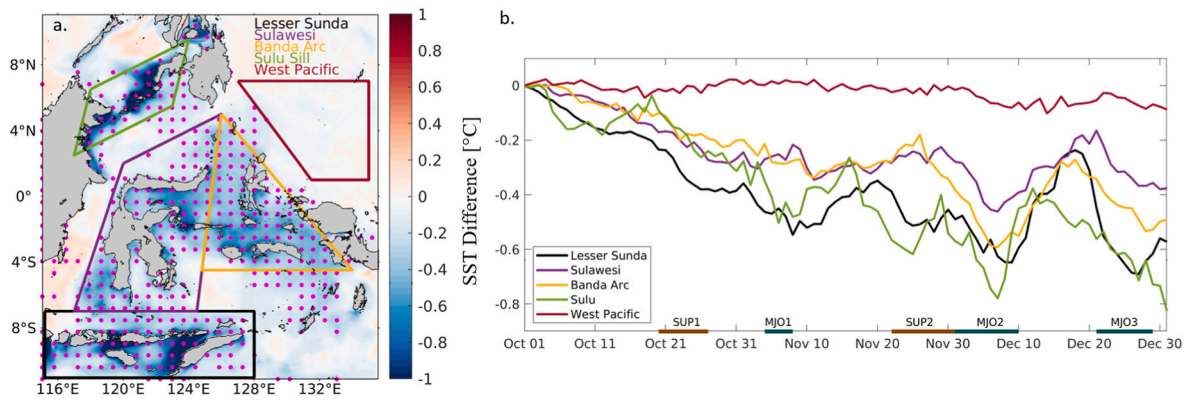
Fig. 5. (a) Ensemble-average SST difference (TIDES - NOTIDES) averaged for Nov.–Dec. 2011, with regional polygons denoting the areas with the strongest SST cooling. Magenta grid points indicate statistically significant cooling due to tidal forcing. (b) Daily time-series of SST differences averaged in each respective region.
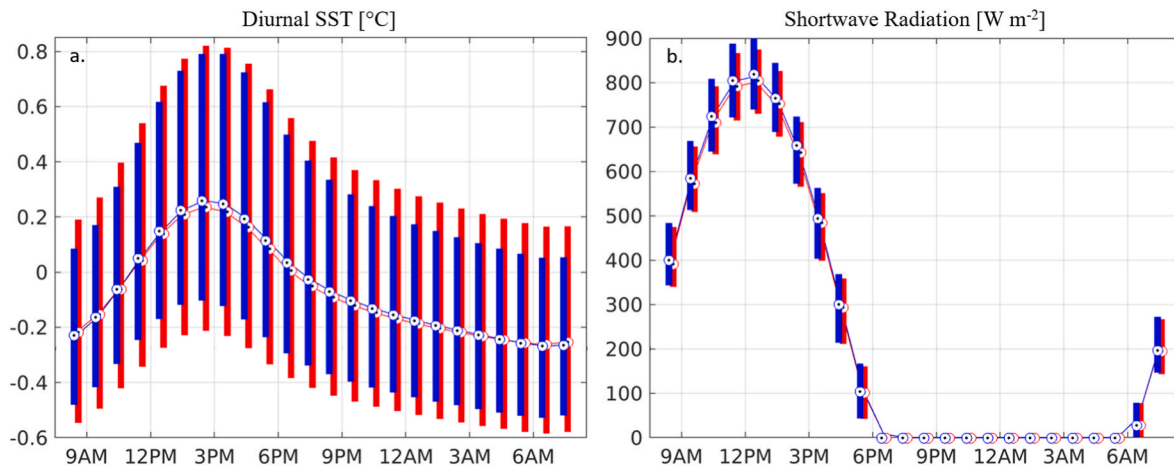

Fig. 6. (a) Box plots of the diurnal cycle of SSTs for TIDES (blue) and NOTIDES (red) ensembles indicating the median values (lines) and the 25th/75th quartiles (bottom/top of bars). (b) Same as in a. but for shortwave radiation.

stratification directly above it. The largest ocean temperature differences associated with tidal mixing in the eastern MC region occur in the subsurface, below the mixed layer, resulting in widespread shoaling of the mixed layer (Fig. 8). The depth at which tidal cooling is maximized is site-specific, generally occurring near the base of the mixed layer. Regions displaying strong tidal mixing signatures (Fig. 5) have average mixed layer depths (MLDs) of 10–15 m. The MLD is calculated using a threshold method with a density criterion of 0.125 kg m^{-3} from a 5-m reference depth (de Boyer Montégut et al., 2004). In the TIDES ensemble, all eastern MC regions have the largest MLD shoaling of ~3 m (Fig. 8). These regions display the strongest SST cooling responses to tidal mixing. In contrast, the open ocean of the west Pacific region has the deepest MLDs of ~20 m, where minimal tidal mixing produces small changes in MLD between the TIDES and NOTIDES ensembles.

For example, in the Banda Arc region near Maluku (126.5°E, 2.5°S), where the tidal impacts on SST are strong, the subsurface ocean temperatures between the TIDES and NOTIDES experiments differ by more than 2.5 °C at a depth of ~40–50 m (Fig. 9a). However, the subsurface cooling remains relatively undisturbed during 21–30 November, corresponding to the suppressed phase of MJO (phases 2–3) under the calmer zonal wind. This enhanced subsurface cooling during the suppressed phases of MJO results in increased near-surface stratification, as measured by the Brunt-Väisälä frequency, directly above the region of subsurface cooling (Fig. 9b). Due to weak vertical mixing under low wind conditions, the near-surface stratification is maintained, effectively decoupling the tidally-driven subsurface cooling from the surface. This results in minimal SST cooling (Fig. 9c) during the suppressed phase

of MJO2.

During the active phase of MJO2 (phases 4–5, December 1–10), in contrast, the enhanced wind-driven mixing under the increased westerly winds (Fig. 9e) erodes the near-surface stratification (Fig. 9d), enabling vertical mixing of the tidally-driven colder water mass at the base of the mixed layer into the surface layer (Fig. 9c). Indeed, local SST cooling in TIDES during the active phase exceeds ~1 °C in marked contrast during the suppressed phase. Hence, the tidal rectification of the subsurface ocean temperatures and the subsequent shoaling of the mixed layer (Fig. 9f) manifests more strongly in the SST during the active phase of MJO. The relationship between tidally-driven ocean cooling and the MJO phase would benefit from a longer model integration period encapsulating a larger sample of MJO events, but this is beyond the scope of the study. Its implication to the intraseasonal precipitation variability is discussed in Section 4.3.

4. Atmospheric response to tidal cooling

4.1. Time-mean atmospheric responses

The time-mean SST cooling seen in the previous section is accompanied by the consistent spatial changes in latent and sensible heat fluxes (LHF/SHF, defined as positive into the ocean, Fig. 10a), near-surface humidity, and temperature (Fig. 8b and c), as well as atmospheric convection as indicated by outgoing longwave radiation (OLR, Fig. 10d). The time-mean LHF is negative, resulting in warming and moistening of the atmosphere (not shown). In the TIDES experiment,
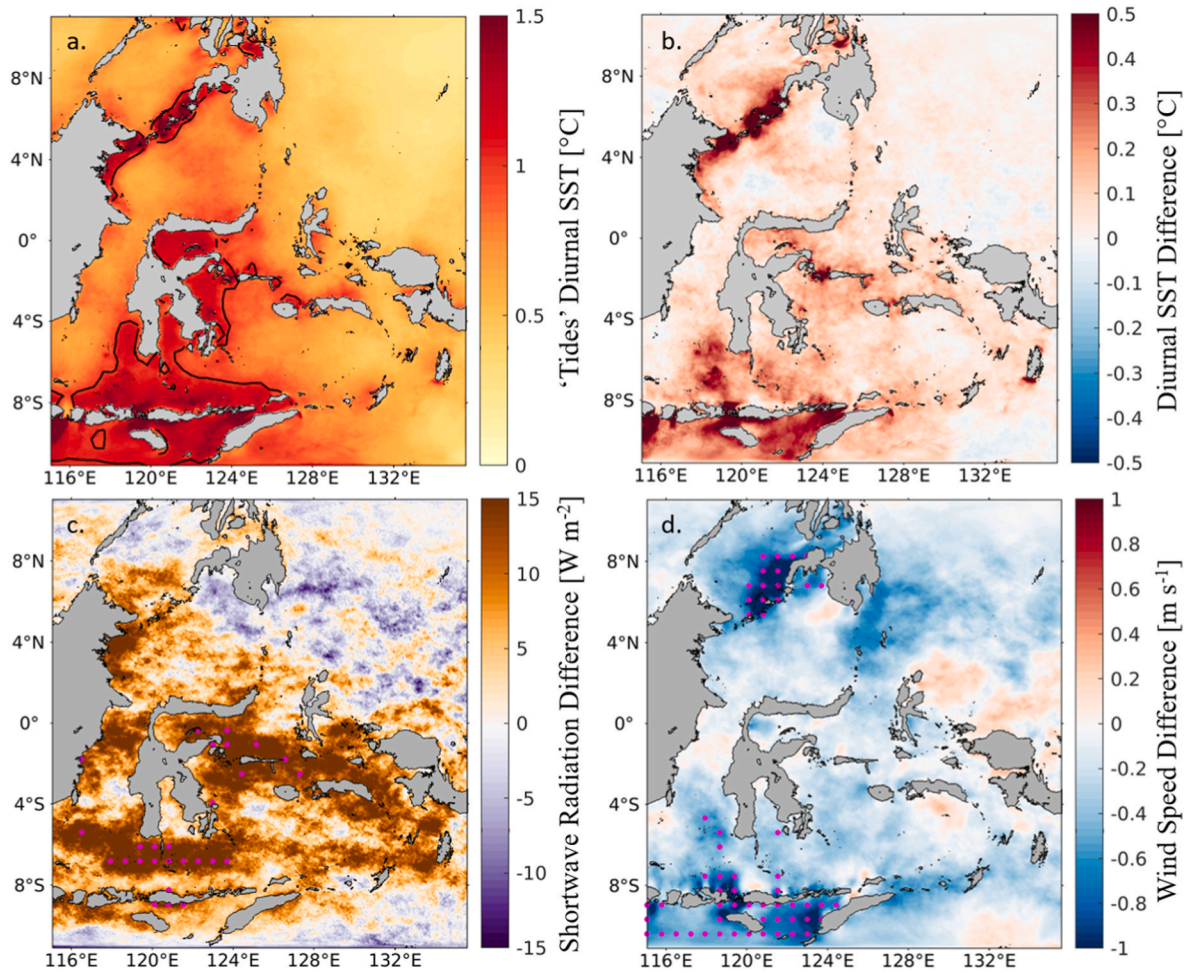
Fig. 7. Spatial plot of time-averaged, diurnal cycle amplitude of SST with 1 °C contour (black) for (a) TIDES ensemble and (b) the difference between TIDES and NOTIDES ensembles. The spatial plot of time-averaged differences in (c) shortwave radiation and (d) wind speed between TIDES and NOTIDES ensembles, where magenta dots indicate statistically significant differences at the 95% confidence interval.
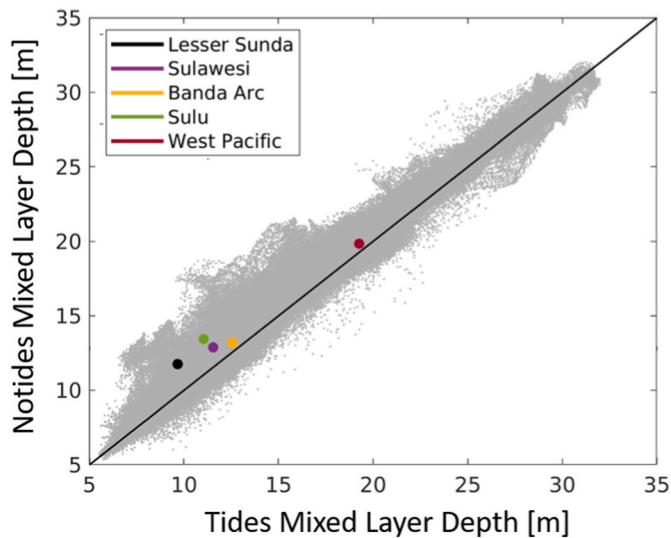

Fig. 8. Scatter plot comparison of mixed layer depth (MLD) between the TIDES and NOTIDES experiments. Each grid point in eastern MC is shown (gray points), along with regional averages for Lesser Sunda (black), Sulawesi (purple), Banda Arc (orange), Sulu Sill (green), and Western Pacific (red).

one can find the reduction in LHF (i.e., anomalous ocean warming or anomalous atmospheric cooling/drying) by more than 10%, which mitigates the SST cooling induced by the tides. The reduced LHF out of the ocean is due to a decreased saturation water vapor mixing ratio over the tidally-cooled SST (not shown), leading to lower near-surface humidity (Fig. 10b) and temperature (Fig. 10c). These changes in near-surface meteorology and turbulent heat fluxes are consistent with the weakened atmospheric convective activity, as seen from the increase in time-mean OLR (Fig. 10d).

As indicated by the reduced convective activity, the impact of the SST cooling by tides is not limited only to the surface layer, but reaches the troposphere. A column-integrated moist static energy (MSE) time series shows that the TIDES ensemble has a slight, but measurable reduction in column-integrated MSE (Fig. 11a). The spatial distribution shows a broad decrease in column-integrated MSE over the eastern MC for the TIDES ensemble, with statistically significant differences centered around Sulawesi (Fig. 11b). A predominantly drier atmospheric column in the TIDES ensembles contributes to the differences in column-integrated MSE. The drier, lower-to mid-level atmosphere (not shown) is consistent with the reduction in regional rainfall shown in Fig. 12.

The most intense rainfall rates of nearly 2 mm h^{-1} occur inland of large islands (i.e., Sulawesi) within the MC (Fig. 12a), where land-sea breezes and orographic enhancement drive a robust diurnal cycle of convection. Due to the chaotic nature of tropical convection, precipitation rate fields are spatially smoothed with a 10-point filter, which
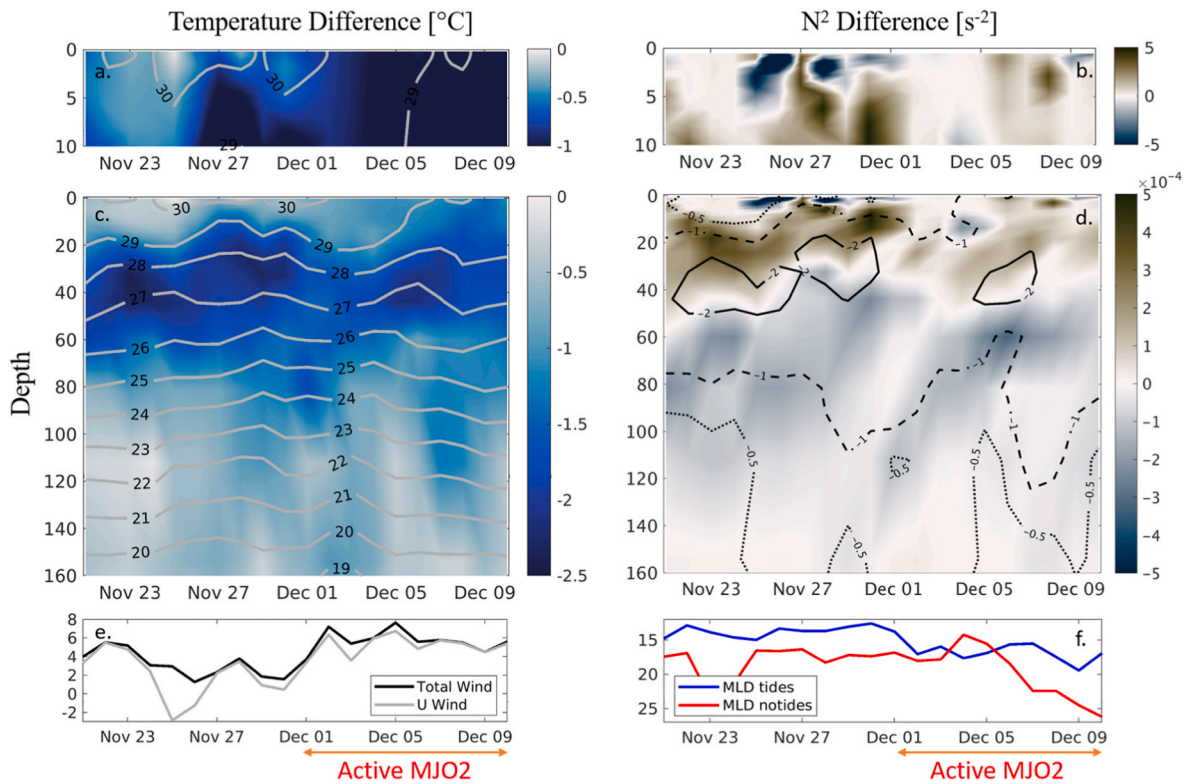
Fig. 9. Depth-time cross-sections at 126.5°E, 2.5°S within the Banda Arc region of near-surface (0–10 m depth) (a) ocean temperature difference (°C) and (b) stratification difference (s^{-2}) between TIDES and NOTIDES, and a deeper (c.-d.) view from the surface to 160 m depth, respectively. The time period covers the suppressed (Nov. 21–30) and active (Dec. 01–09) phases of the MJO2 event. Ocean temperatures in TIDES are contoured every 1 °C (a., gray contours), and temperature differences (b., TIDES-NOTIDES) are contoured at −2 °C (solid black), −1 °C (dashed black), and −0.5 °C (dotted black). For reference, the coincident time series of (e.) zonal and total wind speeds and (f.) mixed layer depths for TIDES and NOTIDES are plotted.

reduces the spatial resolution to ~40 km. Generally, the SST reduction resulting from tidal mixing has a limited impact on land-based precipitation, especially in the inner parts of the large islands. In contrast, a more substantial decrease in rainfall tends to be located in the coastal regions of the enhanced SST cooling, most notably near Sulawesi, the Banda Arc, and the Sulu Sill (Fig. 12b).

4.2. Changes to diurnal precipitation

In addition to the drier atmospheric column and reduced regional precipitation in the MC, the tidally-induced SST cooling also influences the diurnal characteristics of regional precipitation. The diurnal composite evolution of TRMM precipitation rates is compared to that of TIDES during different periods of the diurnal cycle: 00Z, 06Z, 12Z, and 18Z (Fig. 13). It should be noted that satellite-derived precipitation rates are less reliable over steep topography and along coastal regions. Land-based precipitation from TRMM (Fig. 1a–d) initiates along the coastlines in the early afternoon hours, near 06Z, and subsequently propagates offshore, peaking at the coastal oceans in the early-morning hours around 00Z. The simulated precipitation from TIDES (Fig. 13e–h) tends to initiate too early and too vigorously compared to TRMM, a feature that is also seen in previous high-resolution modeling studies with comparable resolution (Love et al., 2011; Vincent and Lane, 2016; Hassim et al., 2016; Li et al., 2017). Indeed, the model has a high precipitation bias at all times throughout the diurnal cycle (Fig. 13i–l), with the largest bias occurring during the daytime maximum over land, where TIDES produces double the satellite-based precipitation estimates (Fig. 14a vs. 12b). In contrast, the bias in sea-based precipitation is much weaker at ~0.1 mm h^{-1}. Despite the bias in the diurnal precipitation magnitude, the timing and the spatial pattern of the diurnal precipitation are reasonably well simulated. For example, the daytime maximum

in land-based precipitation occurs around 14Z both in TIDES (Fig. 14a) and satellite-based estimates from TRMM and CMORPH (Fig. 14b). In addition, the spatial pattern of precipitation rates between the two is largely consistent (Fig. 13). Furthermore, sea-based precipitation from the model peaks in the early-morning hours from 03Z to 06Z and is considerably less than the daytime maximum peak, as seen in TRMM. Finally, the largest early-morning precipitation is concentrated along the coastlines of Sumatra, Java, Borneo, Sulawesi, and West New Guinea.

Regarding the sensitivity of the diurnal precipitation to the tide-induced SSTs, the lower SST in TIDES alleviates the high precipitation bias over the oceans. Because the SST cooling is enhanced in the near-shore and coastal zones, the more prevalent reduction in precipitation is found over the coastal oceans, while a more modest reduction occurs over land (Fig. 15). On average, the high bias in precipitation rates from WRF is improved, and total precipitation is reduced by ~11%.

The strongest reduction in diurnal precipitation in TIDES occurs in the early-to mid-morning between 18Z and 00Z near Sulawesi (Fig. 15). Over coastal ocean grid points with an enhanced tidal SST cooling signature (Fig. 5), the reduction of precipitation rates by upwards of 0.4 mm h^{-1} is commonly observed, representing a 25–40% modulation of precipitation at some coastal ocean grid points. The imprints of the near-coastal SSTs in the diurnal convection appear near 12Z as land-based convection wanes and begins to propagate offshore. The signal of reduced precipitation rates along the coast continues to propagate offshore at 18Z and 00Z before subsiding around 06Z. On average, there is a 20.4% reduction of the daily-mean rainfall by tidally-induced cooler SST over the shallow, coastal seas (Table 2).

Furthermore, while land-based diurnal convection peaks in the mid-afternoon near 06Z–07Z with maximum precipitation rates >2 mm h^{-1} in all islands in the eastern MC, the land-based precipitation response to
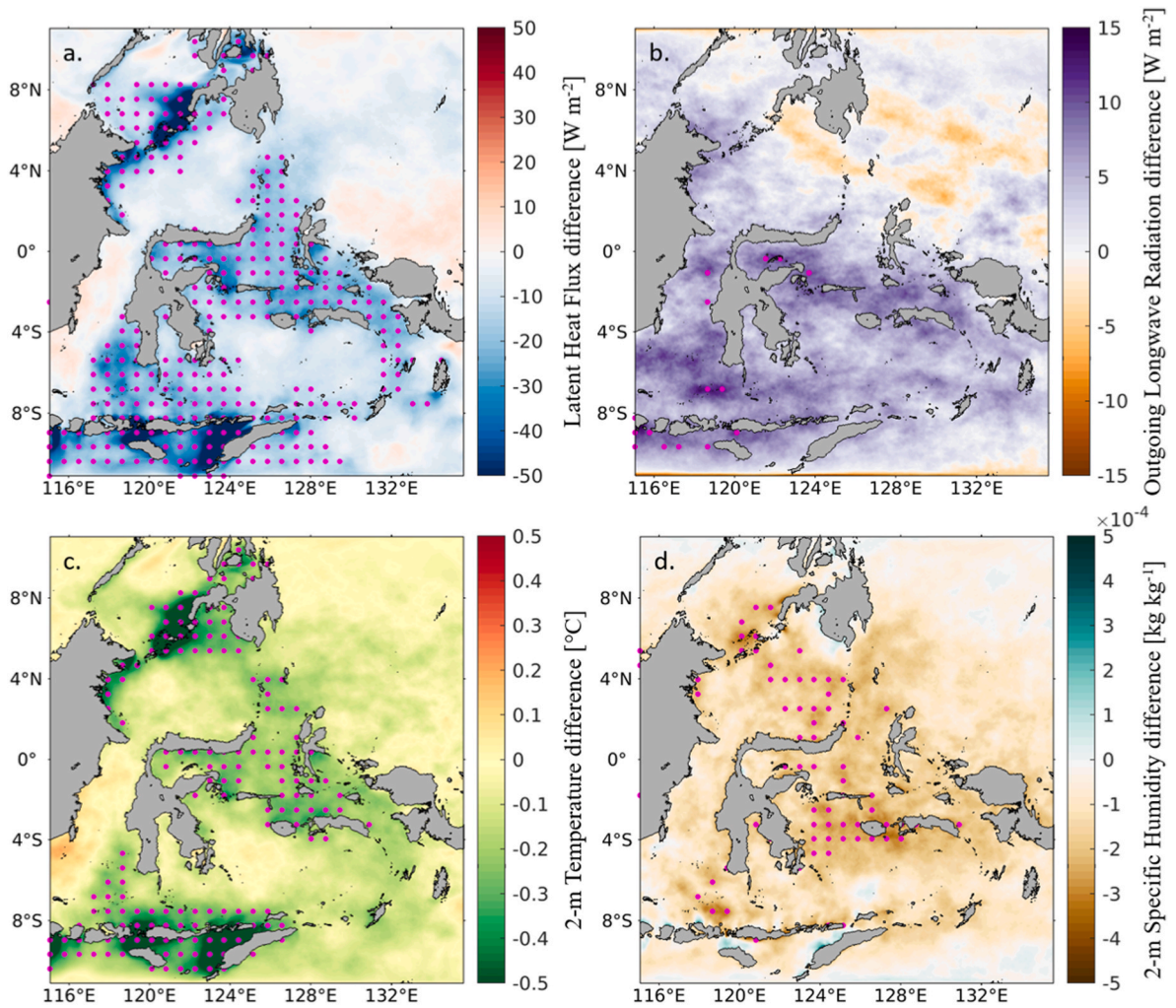
Fig. 10. Near-surface meteorological response differences between the TIDES and NOTIDES experiments: (a) latent heat flux (LHF, W m^{-2}, positive into the ocean), (b) outgoing longwave radiation, (OLR, W m^{-2}), (c) 2-m air temperature ($^{\circ}$C), and (d) 2-m specific humidity (kg kg^{-1}) where magenta dots indicate statistically significant differences at the 95% confidence interval.
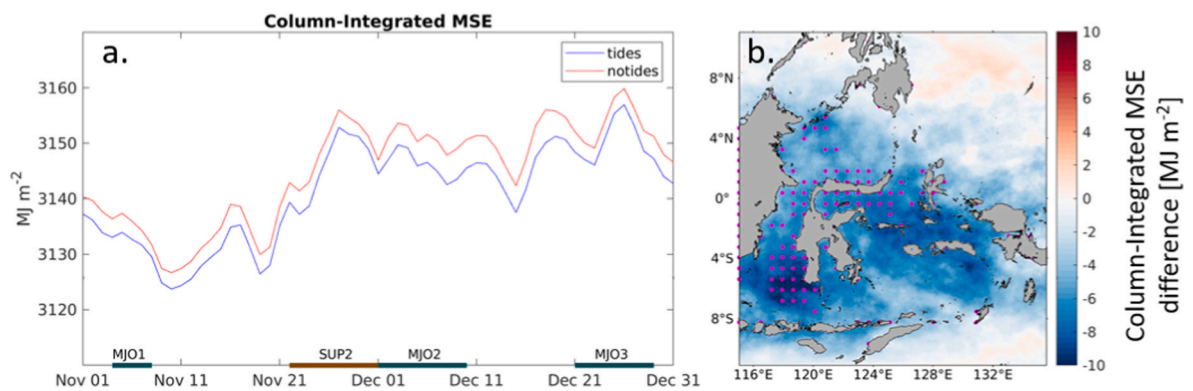

Fig. 11. (a) Time series of column-integrated MSE for TIDES (blue) and NOTIDES (red) ensembles, where suppressed (brown) and active (green) phases of MJO within the MC are indicated along the x-axis. (b) The two-month average of column-integrated MSE differences between TIDES and NOTIDES ensembles (blue shading indicates column-integrated MSE for TIDES is less than NOTIDES), where magenta dots indicate statistically significant differences at the 95% confidence interval.

the nearshore and coastal SST cooling is apparent only in smaller islands such as Maluku, rather than large islands such as Sulawesi. For example, one finds no coherent reduction of late afternoon diurnal convection over Sulawesi, yet there is a robust decrease over Maluku.

In summary, the eastern MC shows a robust reduction in diurnal precipitation to tidally-modulated SST cooling, most strongly manifested in the nearshore and coastal oceans where the tide-induced SST cooling is strongest, and also between 18Z-0Z when the land-based
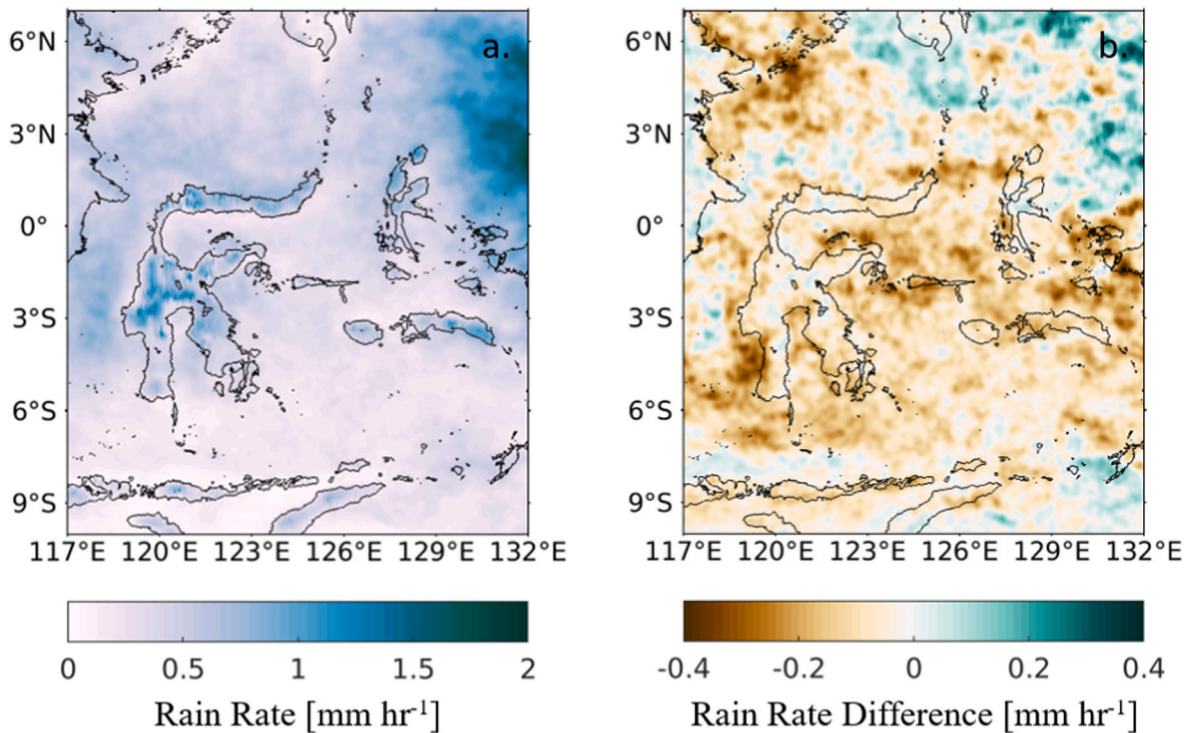
Fig. 12. Ensemble mean of (a) WRF rain rate from TIDES and (b) rain rate difference between TIDES and NOTIDES over the eastern MC, averaged from Nov.–Dec. 2011.

convection directly overlies the cooler coastal oceans (Table 2).

4.3. Interactions with MJO-scale processes

In Section 3.2, it was suggested that the magnitude of the SST cooling resulting from tides co-varies with the MJO phase. The stronger SST cooling occurs during active phases of MJO because of the combined action of the tide-induced subsurface cooling and the wind-driven mixing by the MJO winds. In contrast, the near-surface stratification is enhanced, and SST change is small or even opposite with tides during the suppressed phase due to the tide-induced subsurface cooling. This indicates that semi-diurnal tidal forcing is connected to intraseasonal SST variability at MJO time-scales. To further investigate these relationships and the subsequent impacts, a 10-30-day bandpass filtering is applied to the area-averaged SST anomalies (SSTa) and precipitation rate anomalies (PRCPa) in each of the experiments. The 10-30-day bandpass filter was selected due to the relatively short three-month model integration period, while still capable of extracting the higher-frequency end of the MJO signal. Though the time-mean responses are removed via bandpass filtering, the changes in SSTa and PRCPa co-variability, the focus of this analysis, can be detected due to the recti-fied changes in the mean state of the upper oceans (i.e., colder subsur-face ocean temperature).

During the study period, there are four instances where the bandpass filtered SSTa in both TIDES and NOTIDES ensembles surpasses the +1 standard deviation (std, 0.1 °C, thin straight lines) (Fig. 16a). The final three SSTa peaks occur before the onset of active MJOs. The bandpass filtered SSTa from TIDES shows larger peak-to-trough amplitude during the first and second MJO events (the so-called MJO1 and MJO2, respectively), characterized by enhanced SST warming during the sup-pressed phases, followed by the more substantial SST cooling during active phases. This result is consistent with the upper ocean analysis (Section 3.2), where the TIDES ensemble exhibits anomalously enhanced stratification during the suppressed phase and the penetrative wind-driven vertical mixing leading to cooler SSTs during the active

phase.

Similarly, several peaks and troughs in the intraseasonal PRCPa time series are concurrent with the active and suppressed phases of MJO, respectively (Fig. 16b). During MJO1, the peak PRCPa does not exceed the +1 std threshold in NOTIDES. Also, the length of PRCPa extends beyond the MJO1 period during the first week of November (defined by the Wheeler-Hendon index, Wheeler and Hendon, 2004). However, both MJO2 and MJO3 active phases are clearly defined in the time series, where the percent difference of PRCPa in TIDES is 228% and 164% greater than NOTIDES at peak activity. Hence, the stronger PRCPa during the peak of convection in TIDES is preceded by the warmer SSTa during the suppressed phase. This result suggests that the intensity of the intraseasonal precipitation anomalies in the MC is modulated by the tidal effects on upper ocean stratification and SST during the MJO suppressed phases.

The intensity changes of the intraseasonal coupling between SSTa and PRCPa are further examined based on their cross-correlation. The cross-correlation between SSTa and PRCPa (Fig. 16c) reaches ±0.5 in TIDES, but only ± 0.2 in NOTIDES. The phasing is generally consistent between the two experiments, where positive correlations occur when SSTa leads by PRCPa by 6–8 days and negative correlation when SSTa lags PRCPa by 3–4 days. Comparing the quadrature relationship be-tween SSTa and PRCPa indicates that the extent to which the SST and precipitation are coupled at intraseasonal timescales is enhanced with tides.

The enhanced intraseasonal coupling between SSTa and PRCPa in TIDES can be explained in the framework of the recharge-discharge paradigm (Bladé and Hartmann, 1993; Benedict and Randall, 2007), with the modification considering the asymmetric role of tidally-driven SST responses in different MJO phases. That is, during the recharge periods of the MJO suppressed phase, the moisture in the lower atmo-sphere is accumulated over the warm SST during the calm and sunny period. Because of the weak wind, the strong subsurface cooling by the tides is capped by the near-surface stratification and does not cool the SST as effectively. This is conducive to anomalous warming of SST and
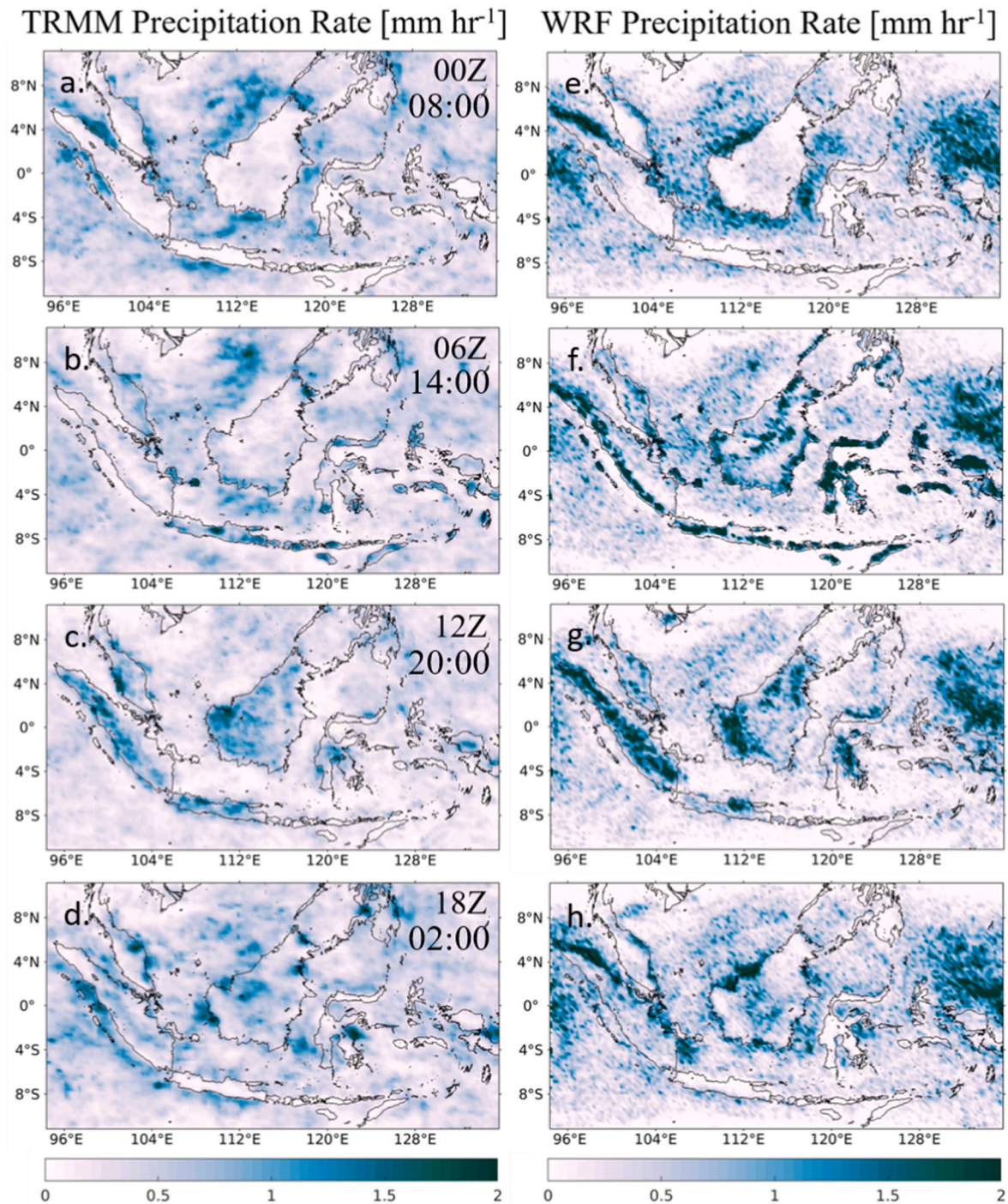
Fig. 13. Diurnal cycle of average precipitation rates at 00Z (08:00 local), 06Z (14:00 local), 12Z (20:00 local), and 18Z (02:00 local) from TRMM (a.-d.) and WRF ensemble averages from TIDES (e.-h.).

moistening of the troposphere before convection, followed by further moistening of the troposphere by deep convection (e.g., Benedict and Randall, 2007; Haertel et al., 2008). Then, during the discharge period of the MJO active phase, anomalous zonal winds at the surface enhance wind-driven mixing of the upper ocean. The deepened mixed layer connects the tidally-driven subsurface cooling to the surface, leading to a more robust SST cooling response. In this capacity, the magnitude of the intraseasonal SSTa and PRCPa are both enhanced, as well as the strength of their quadrature relationship in the TIDES experiment.

5. Conclusions

The MC region is characterized by strong tidal mixing, concentrated near complex bathymetric features. Tide gauge observations from UHSLC show strong semi-diurnal to diurnal fluctuations in sea level driven by the tides. The frequency characteristics of the modeled tides accurately simulate sea level variability in the MC compared to these observations. The resulting water mass transformation of the upper ocean along the ITF pathways modifies the SST distribution across the eastern MC, impacting the regional climate and tropical convection. The time-mean SSTs over the eastern MC are reduced by 0.20 °C in the TIDES
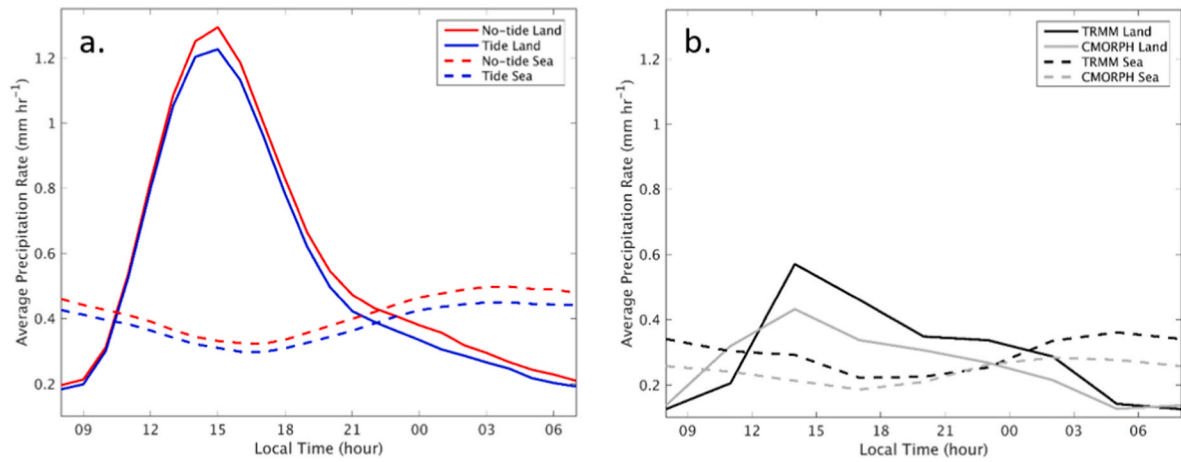
Fig. 14. (a) Diurnal cycle of average precipitation rates over land (solid) and sea (dashed) from TIDES (blue) and NOTIDES (red) compared to (b) satellite-based observations from TRMM (black) and CMORPH (gray).
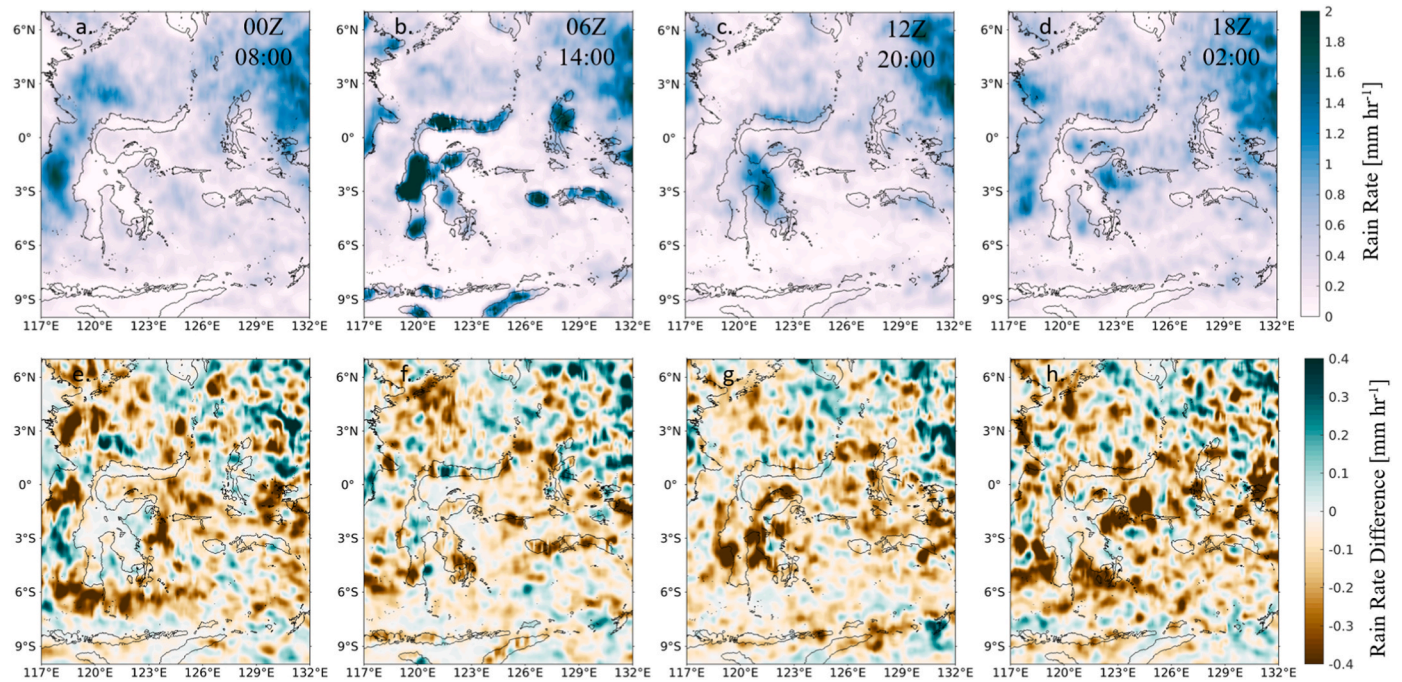

Fig. 15. Time-mean, ensemble-mean WRF precipitation rate from TIDES throughout the diurnal cycle at (a) 00Z (08:00 local), (b) 06Z (14:00 local), (c) 12Z (20:00 local), and (d) 18Z (02:00 local). The precipitation rate difference between TIDES and NOTIDES ensembles at the same diurnal times (e–h).

Table 2
Changes in diurnal precipitation [mm hr^{-1}] between TIDES (top), NOTIDES (middle), and percent (%) difference (bottom) over the land, shallow sea (0–1000 m), and deep-sea (>1000 m) locations. Statistically significant differences using a two-sample Students' *t*-test at the 95% significance level are indicated by bold text.

Time (UTC/Local)	00Z/0800	03Z /1100	06Z/1400	09Z/1700	12Z/2000	15Z/2300	18Z/0200	21Z/0500	Total
Land-based Precipitation	0.18	0.54	1.26	1.00	0.54	**0.38**	**0.29**	**0.22**	**0.55**
	0.20 (−12.9)	0.58 (−6.9)	1.33 (−5.3)	1.07 (−6.9)	0.59 (−10.0)	**0.45 (-16.9)**	**0.34 (-19.5)**	**0.25 (-16.3)**	**0.60 (-9.4)**
Shallow sea-based precipitation	**0.35**	0.30	**0.25**	**0.24**	**0.28**	**0.36**	**0.39**	**0.38**	**0.32**
	0.41 (-19.0)	0.35 (−17.4)	**0.30 (-21.3)**	**0.28 (-20.8)**	**0.34 (-22.8)**	**0.43 (-20.7)**	**0.47 (-20.3)**	**0.45 (-20.5)**	**0.38 (-20.4)**
Deep sea-based precipitation	0.52	0.47	0.39	0.36	0.41	0.48	0.53	0.54	**0.46**
	0.56 (−8.4)	0.51 (−7.3)	0.41 (−5.9%)	0.39 (−8.2)	0.44 (−7.5)	0.52 (−8.1)	0.57 (−7.7)	0.59 (−8.8)	**0.50 (-7.9)**

ensemble, with localized cooling exceeding 1 °C in the regional tidal hotspots near Lesser Sunda Islands, Sulawesi, the Banda Arc, and the Sulu Sill. When warm SSTs are present throughout the MC in austral summer, small changes in SST across the convective threshold can influence deep convection at a range of time-scales, including diurnal precipitation and intraseasonal modes like MJO. We demonstrate that ocean tides generate a consequential SST cooling of 0.2 °C in the MC, and their coupled effects are manifested across a range of scales to influence oceanic and atmospheric variability. The scale and magnitude of the SST response to tidal forcing and the associated ~20% reduction in
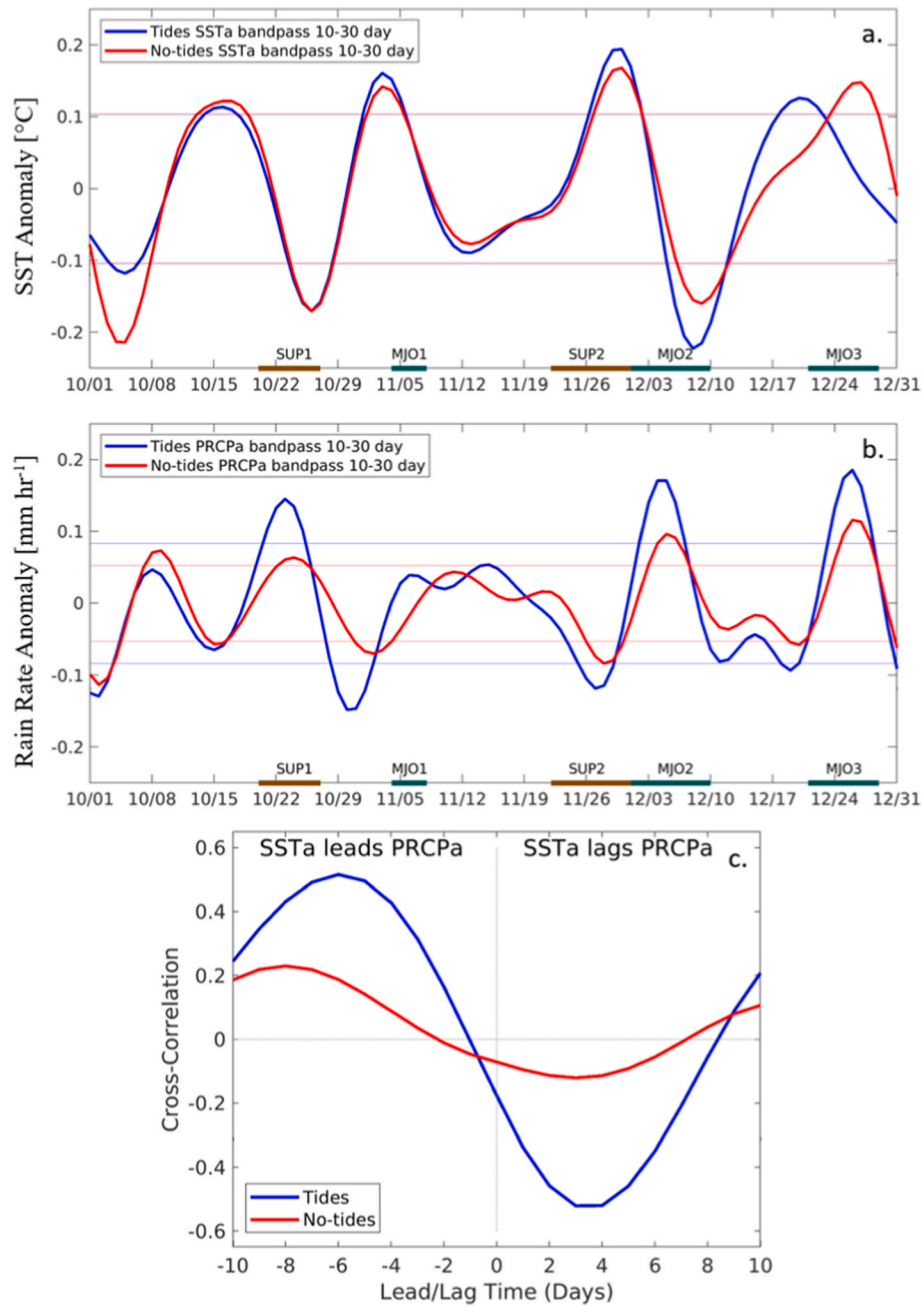
Fig. 16. (a) Time series of 10-30-day bandpass filtered SST anomaly and (b) rain rate anomaly to highlight MJO-scale interaction and variability within the eastern MC. The time series is composed of the ensemble averages of the TIDES (blue) and NOTIDES (red) runs with ±1 standard deviation shown. (c) Cross-correlation between 10 and 30 day bandpass filtered SST anomaly (SSTa) and rain rate anomaly (PRCPa).

convection near the coastlines are consistent with prior coupled modeling studies of parameterized tides in the MC (Koch-Larrouy et al. 2010; Sprintall et al., 2014).

In the upper oceans, the most robust temperature response to tides occurs below the base of the mixed layer, where subsurface cooling can surpass 2.5 °C, as evident in the Banda Arc location. On the regional scale, there is widespread shoaling of the mixed layer depth throughout the MC due to this subsurface cooling driven by the tides. Above the layer of maximum cooling, thermal stratification is enhanced, causing the mixed layer to shoal. Strengthened westerly winds associated with active MJO phases generate vertical mixing that penetrates the thermocline and effectively mixes the cooler, subsurface waters to the surface. Conversely, during suppressed phases of MJO, surface wind forcing is weak, and cooler thermocline water is unable to mix toward the

surface. Through this mechanism, we demonstrate that tidal mixing can affect the local MJO-SST coupling within the MC.

Another notable finding is that the time-mean reduction in SST from tidal forcing in the eastern MC is similar in magnitude to intraseasonal SST anomalies associated with MJO passage and, therefore, may be consequential for local MJO maintenance in this region. The complex, nonlinear interactions that govern MJO variability and propagation are modulated by a moisture mode (Wang et al., 2016), where the zonal mean moisture gradient is known to drive the eastward MJO propagation (Kim et al., 2014). Coupled ocean-atmosphere processes aid preconditioning and moisture convergence eastward of the main convective envelope, which helps to sustain the MJO (DeMott et al., 2019). The effects of tidal mixing via modulation of regional SST cooling and drying of the atmosphere over the eastern MC may influence or disrupt local

MJO propagation across the MC.

The results show that the surface atmospheric response is consistent with tidally-induced SST cooling; namely, there is a reduction in latent heat flux, specific humidity, and air temperature. Atmospheric drying extends throughout the troposphere, and column-integrated MSE is noticeably reduced in the TIDES ensemble. The largest decreases in column-integrated MSE are centrally located within the MC, near Sulawesi. The changes in near-surface meteorological fields are consistent with the weakened atmospheric convective activity, as demonstrated by an increase in OLR and decrease in precipitation. Regional precipitation in the eastern MC is reduced by 11%, thereby alleviating some of the high bias in modeled precipitation.

The tidally-induced SST cooling modifies the diurnal characteristics of regional precipitation. The diurnal cycle of convection is driven by daytime heating over MC islands, leading to a peak in land-based precipitation in the late-afternoon to early-evening hours. Since daytime convection over land is supported by strong thermodynamic forcing, the remote effect of SST cooling near the coasts is weak on land-based precipitation. At the diurnal peak, average precipitation rates over land are 1.26 mm h^{-1} in the TIDES ensemble, corresponding to only a 5.3% reduction from NOTIDES. Interestingly, during the late-evening and early-morning hours, when land-based precipitation subsides, there is a statistically significant reduction in precipitation rates over land. In the absence of strong diurnal forcing, the overall drying of the atmosphere is likely responsible for the reduced precipitation rates from 2300 to 0500 local time. Diurnal convective activity propagates offshore during the early-morning hours and directly interacts with cooler SSTs near the coast. Since SST cooling in response to tidal forcing is more prevalent near the coast, the largest reduction in precipitation of 20.4% also occurs over shallow, coastal seas. The tidal effects on SSTs and reduced precipitation weaken in these tidal hotspots. However, there is still a statistically significant decrease in time-mean precipitation rates over the deeper, interior seas of the MC.

The impact of the tides also modulates the coupling between intraseasonal SST variability and local MJO activity across the MC. The magnitude of tide-induced SST cooling co-varies with the MJO phase, where active phases of MJO induce (and then respond to) a stronger SST cooling response. By bandpass filtering the SSTa and PRCPa at MJO time-scales, we find a stronger intraseasonal SSTa-PRCPa coupling in TIDES. For both MJO2 and MJO3 events, TIDES shows higher SSTa and weaker convection during the suppressed phase, followed by cooler SSTa and stronger convection during the active phase, consequently enhancing the intraseasonal ocean-atmosphere coupling in TIDES. The physical mechanism responsible for this might be explained by the modified context of the recharge-discharge paradigm with the inclusion of the asymmetric role of tides in SST response to local MJO. During MJO suppressed phases, as the mixed layer is shallower and more stratified at its base in TIDES, the surface ocean is insulated from the cooler subsurface and can become warmer in response to incoming solar radiation. Higher pre-convection SSTs drive higher surface heat fluxes out of the oceans and preconditions the lower troposphere. The anomalous moistening of the atmosphere prior to MJO leads to higher pre-cipitation amounts during the discharge period. Anomalously strong zonal winds associated with MJO passage during the active phase can generate strong turbulent mixing to entrain cooler subsurface water toward the surface. As a result, the coupling between intraseasonal SSTa and PRCPa is strengthened due to tidal forcing.

There are several caveats in the analyses presented in this study. Robust identification of the responses in deep convection and circulation remains challenging in this short set of simulations with a small ensemble size. The high computational expenses of running the coupled ocean-atmosphere model at convection-permitting scales preclude us from running a long-term simulation or large ensembles of MJO cases. Future modeling studies with a large sample of MJO events or more ensemble members are needed to quantify the phase-dependent nature of tidal SST cooling related to localized MJO within the MC. However,

since there is reasonable confidence about the time-mean reduction in SST due to tidal forcing in the ocean and given the importance of the background humidity state in the propagation of the local MJO in the MC (e.g., Gonzalez and Jiang, 2017; Jiang, 2017; DeMott et al., 2019), it is reasonably anticipated that the inclusion of tidal forcing in such extended high-resolution coupled modeling simulations would also yield the similar responses to tides as presented in this study.

CRediT author statement

John Steffen: Conceptualization, Methodology, Formal analysis, Writing – Original Draft, Visualization.

Hyodae Seo: Conceptualization, Methodology, Software, Validation, Resources, Writing – Original Draft, Funding acquisition.

Carol Anne Clayson: Conceptualization, Data Curation, Writing – Review & Editing.

Suyang Pei: Conceptualization, Methodology, Writing – Review & Editing.

Toshiaki Shinoda: Writing – Review & Editing, Project administration, Funding acquisition.

Declaration of competing interest

The authors declare that they have no known competing financial interests or personal relationships that could have appeared to influence the work reported in this paper.

Data availability

Data will be made available on request.

Acknowledgments

References

Adames, Á.F., Wallace, J.M., 2014. Three-dimensional structure and evolution of the MJO and its relation to the mean flow. J. Atmos. Sci. 71, 2007–2026. https://doi.org/10.1175/JAS-D-13-0254.1.

Adames, Á.F., Kim, D., 2016. The MJO as a dispersive, convectively coupled moisture wave: theory and observations. J. Atmos. Sci. 73, 913–941. https://doi.org/10.1175/JAS-D-15-0170.1.

Aldrian, E., Sein, D., Jacob, D., Gates, L.D., Podzun, R., 2005. Modelling Indonesian rainfall with a coupled regional model. Clim. Dynam. 25, 1–17. https://doi.org/10.1007/s00382-004-0483-0.

Alford, M.H., Gregg, M.C., Ilyas, M., 1999. Diapycnal mixing in the Banda Sea: results of the first microstructure measurements in the Indonesian throughflow. Geophys. Res. Lett. 26, 2741–2744. https://doi.org/10.1029/1999GL002337.

Argüeso, D., Romero, R., Homar, V., 2020. Precipitation features of the Maritime continent in parameterized and explicit convection models. J. Clim. 33, 2449–2466. https://doi.org/10.1175/JCLI-D-19-0416.1.

Benedict, J.J., Randall, D.A., 2007. Observed characteristics of the MJO relative to maximum rainfall. J. Atmos. Sci. 64, 2332–2354. https://doi.org/10.1175/JAS3968.1.

Bladé, I., Hartmann, D.L., 1993. Tropical intraseasonal oscillations in a simple nonlinear model. J. Atmos. Sci. 50, 2922–2939. https://doi.org/10.1175/1520-0469(1993)050<2922:TIOIAS>2.0.CO;2.

Chen, F., Dudhia, J., 2001. Coupling an advanced land surface–hydrology model with the penn state–NCAR MM5 modeling system. Part I: model implementation and sensitivity. Mon. Weather Rev. 129, 569–585. https://doi.org/10.1175/1520-0493(2001)129<0569:CAALSH>2.0.CO;2.

Ciesielski, P.E., Coauthors, 2014. Quality-controlled upper-air sounding dataset for DYNAMO/CINDY/AMIE: development and corrections. J. Atmos. Ocean. Technol. 31, 741–764. https://doi.org/10.1175/JTECH-D-13-00165.1.

Clayson, C.A., Bogdanoff, A.S., 2013. The effect of diurnal sea surface temperature warming on climatological air–sea fluxes. J. Clim. 26, 2546–2556. https://doi.org/10.1175/JCLI-D-12-00062.1.

Clayson, C.A., Brown, J., 2016. NOAA climate data record ocean surface bundle (OSB) climate data record (CDR) of ocean heat fluxes, version 2. Clim. Algorithm Theor. Basis Doc. C-ATBD Asheville NC NOAA Natl. Cent. Environ. Inf. Doi 10, V59K4885.

Coppin, D., Bellon, G., 2019a. Physical mechanisms controlling the offshore propagation of convection in the tropics: 1. Flat island. J. Adv. Model. Earth Syst. 11, 3042–3056. https://doi.org/10.1029/2019MS001793.

Coppin, D., Bellon, G., 2019b. Physical mechanisms controlling the offshore propagation of convection in the tropics: 2. Influence of topography. J. Adv. Model. Earth Syst. 11, 3251–3264. https://doi.org/10.1029/2019MS001794.

Dee, D.P., Coauthors, 2011. The ERA-Interim reanalysis: configuration and performance of the data assimilation system. Q. J. R. Meteorol. Soc. 137, 553–597. https://doi.org/10.1002/qj.828.

DeMott, C.A., Klingaman, N.P., Tseng, W.-L., Burt, M.A., Gao, Y., Randall, D.A., 2019. The convection connection: how ocean feedbacks affect tropical mean moisture and MJO propagation. J. Geophys. Res. Atmos. 124, 11910–11931. https://doi.org/10.1029/2019JD031015.

de Boyer Montégut, C., Madec, G., Fischer, A.S., Lazar, A., Iudicone, D., 2004. Mixed layer depth over the global ocean: an examination of profile data and a profile-based climatology. J. Geophys. Res.: Oceans 109. https://doi.org/10.1029/2004JC002378.

de Szoeke, S.P., Marke, T., Brewer, W.A., 2021. Diurnal Ocean surface warming drives convective turbulence and clouds in the atmosphere. Geophys. Res. Lett. 48, e2020GL091299 https://doi.org/10.1029/2020GL091299.

Egbert, G.D., Erofeeva, S.Y., 2002. Efficient inverse modeling of barotropic ocean tides. J. Atmos. Ocean. Technol. 19, 183–204. https://doi.org/10.1175/1520-0426(2002)019<0183:EIMOBO>2.0.CO;2.

Fairall, C.W., Bradley, E.F., Rogers, D.P., Edson, J.B., Young, G.S., 1996. Bulk parameterization of air-sea fluxes for tropical ocean-global atmosphere coupled-ocean atmosphere response experiment. J. Geophys. Res.: Oceans 101, 3747–3764. https://doi.org/10.1029/95JC03205.

Fairall, C.W., Hare, J.E., Grachev, A.A., Edson, J.B., 2003. Bulk parameterization of air–sea fluxes: updates and verification for the COARE algorithm. J. Clim. 16, 571–591. https://doi.org/10.1175/1520-0442(2003)016<0571:BPOASF>2.0.CO;2.

Ffield, A., Gordon, A.L., 1992. Vertical mixing in the Indonesian thermocline. J. Phys. Oceanogr. 22, 184–195. https://doi.org/10.1175/1520-0485(1992)022<0184:VMITIT>2.0.CO;2.

Ffield, A., Gordon, A.L., 1996. Tidal mixing signatures in the Indonesian seas. J. Phys. Oceanogr. 26, 1924–1937. https://doi.org/10.1175/1520-0485(1996)026<1924:TMSITI>2.0.CO;2.

Fujita, M, Yoneyama, K., Mori, S., Nasuno, T., Satoh, M., 2011. Diurnal convection peaks over the eastern Indian ocean off Sumatra during different MJO phases. 気象集誌. 第2輯 89A, 317–330. https://doi.org/10.2151/jmsj.2011-A22.

Ge, X., Wang, W., Kumar, A., Zhang, Y., 2017. Importance of the vertical resolution in simulating SST diurnal and intraseasonal variability in an oceanic general circulation model. J. Clim. 30, 3963–3978. https://doi.org/10.1175/JCLI-D-16-0689.1.

Gonzalez, A.O., Jiang, X., 2017. Winter mean lower tropospheric moisture over the Maritime Continent as a climate model diagnostic metric for the propagation of the Madden-Julian oscillation. Geophys. Res. Lett. 44, 2588–2596. https://doi.org/10.1002/2016GL072430.

Gordon, A.L., Coauthors, 2010. The Indonesian throughflow during 2004–2006 as observed by the INSTANT program. Dynam. Atmos. Oceans 50, 115–128. https://doi.org/10.1016/j.dynatmoce.2009.12.002.

Gottschalck, J., Roundy, P.E., Iii, C.J.S., Vintzileos, A., Zhang, C., 2013. Large-scale atmospheric and oceanic conditions during the 2011–12 DYNAMO field campaign. Mon. Weather Rev. 141, 4173–4196. https://doi.org/10.1175/MWR-D-13-00022.1.

Grell, G.A., Dudhia, J., Stauffer, D.R., 1994. A Description of the Fifth-Generation Penn State/NCAR Mesoscale Model (MM5), vol. 128.

Haertel, P.T., Kiladis, G.N., Denno, A., Rickenbach, T.M., 2008. Vertical-mode decompositions of 2-day waves and the Madden–Julian oscillation. J. Atmos. Sci. 65, 813–833. https://doi.org/10.1175/2007JAS2314.1.

Hagos, S., Leung, L.R., Dudhia, J., 2011. Thermodynamics of the Madden–Julian oscillation in a regional model with constrained moisture. J. Atmos. Sci. 68, 1974–1989. https://doi.org/10.1175/2011JAS3592.1.

Hagos, S.M., Zhang, C., Feng, Z., Burleyson, C.D., De Mott, C., Kerns, B., Benedict, J.J., Martini, M.N., 2016. The impact of the diurnal cycle on the propagation of Madden-Julian Oscillation convection across the Maritime Continent. J. Adv. Model. Earth Syst. 8, 1552–1564. https://doi.org/10.1002/2016MS000725.

Haidvogel, D.B., Arango, H.G., Hedstrom, K., Beckmann, A., Malanotte-Rizzoli, P., Shchepetkin, A.F., 2000. Model evaluation experiments in the North Atlantic Basin: simulations in nonlinear terrain-following coordinates. Dynam. Atmos. Oceans 32, 239–281. https://doi.org/10.1016/S0377-0265(00)00049-X.

Hassim, M.E.E., Lane, T.P., Grabowski, W.W., 2016. The diurnal cycle of rainfall over New Guinea in convection-permitting WRF simulations. Atmos. Chem. Phys. 16, 161–175. https://doi.org/10.5194/acp-16-161-2016.

Hatayama, T., 2004. Transformation of the Indonesian throughflow water by vertical mixing and its relation to tidally generated internal waves. J. Oceanogr. 60, 569–585. https://doi.org/10.1023/B:JOCE.0000038350.32155.cb.

Hayes, M.H., 1996. STATISTICAL DIGITAL SIGNAL PROCESSING AND MODELING, vol. 6.

Hong, S.-Y., Noh, Y., Dudhia, J., 2006. A New vertical diffusion package with an explicit treatment of entrainment processes. Mon. Weather Rev. 134, 2318–2341. https://doi.org/10.1175/MWR3199.1.

Ichikawa, H., Yasunari, T., 2006. Time–space characteristics of diurnal rainfall over Borneo and surrounding oceans as observed by TRMM-PR. J. Clim. 19, 1238–1260. https://doi.org/10.1175/JCLI3714.1.

Inness, P.M., Slingo, J.M., 2003. Simulation of the Madden–Julian oscillation in a coupled general circulation model. Part I: comparison with observations and an atmosphere-only GCM. J. Clim. 16, 345–364. https://doi.org/10.1175/1520-0442(2003)016<0345:SOTMJO>2.0.CO;2.

Jiang, X., 2017. Key processes for the eastward propagation of the Madden-Julian Oscillation based on multimodel simulations. J. Geophys. Res. Atmos. 122, 755–770. https://doi.org/10.1002/2016JD025955.

Jiménez, P.A., Dudhia, J., González-Rouco, J.F., Navarro, J., Montávez, J.P., García-Bustamante, E., 2012. A revised scheme for the WRF surface layer formulation. Mon. Weather Rev. 140, 898–918. https://doi.org/10.1175/MWR-D-11-00056.1.

Jin, F., Hoskins, B.J., 1995. The direct response to tropical heating in a baroclinic atmosphere. J. Atmos. Sci. 52, 307–319. https://doi.org/10.1175/1520-0469(1995)052<0307:TDRTTH>2.0.CO;2.

Jochum, M., Potemra, J., 2008. Sensitivity of tropical rainfall to Banda Sea diffusivity in the community climate system model. J. Clim. 21, 6445–6454. https://doi.org/10.1175/2008JCLI2230.1.

Kantha, L.H., Clayson, C.A., 1994. An improved mixed layer model for geophysical applications. J. Geophys. Res.: Oceans 99, 25235–25266. https://doi.org/10.1029/94JC02257.

Kida, S., Wijffels, S., 2012. The impact of the Indonesian Throughflow and tidal mixing on the summertime sea surface temperature in the western Indonesian Seas. J. Geophys. Res.: Oceans 117. https://doi.org/10.1029/2012JC008162.

Kim, D., Coauthors, 2009. Application of MJO simulation diagnostics to climate models. J. Clim. 22, 6413–6436. https://doi.org/10.1175/2009JCLI3063.1.

Kim, D., Kug, J.-S., Sobel, A.H., 2014. Propagating versus nonpropagating Madden–Julian oscillation events. J. Clim. 27, 111–125. https://doi.org/10.1175/JCLI-D-13-00084.1.

Kim, H., Vitart, F., Waliser, D.E., 2018. Prediction of the Madden–Julian oscillation: a Review. J. Clim. 31, 9425–9443. https://doi.org/10.1175/JCLI-D-18-0210.1.

Koch-Larrouy, A., Lengaigne, M., Terray, P., Madec, G., Masson, S., 2010. Tidal mixing in the Indonesian Seas and its effect on the tropical climate system. Clim. Dyn. 34, 891–904. https://doi.org/10.1007/s00382-009-0642-4.

Koch-Larrouy, A., Madec, G., Bouruet-Aubertot, P., Gerkema, T., Bessières, L., Molcard, R., 2007. On the transformation of Pacific Water into Indonesian Throughflow Water by internal tidal mixing. Geophys. Res. Lett. 34 https://doi.org/10.1029/2006GL028405.

Koch-Larrouy, A., Atmadipoera, A., van Beek, P., Madec, G., Aucan, J., Lyard, F., Grelet, J., Souhaut, M., 2015. Estimates of tidal mixing in the Indonesian archipelago from multidisciplinary INDOMIX in-situ data. Deep Sea Res. Oceanogr. Res. Pap. 106, 136–153. https://doi.org/10.1016/j.dsr.2015.09.007.

Kunze, E., Williams III, A.J., Briscoe, M.G., 1990. Observations of shear and vertical stability from a neutrally buoyant float. J. Geophys. Res.: Oceans 95, 18127–18142. https://doi.org/10.1029/JC095iC10p18127.

Li, T., Zhao, C., Hsu, P., Nasuno, T., 2015. MJO initiation processes over the tropical Indian ocean during DYNAMO/CINDY2011. J. Clim. 28, 2121–2135. https://doi.org/10.1175/JCLI-D-14-00328.1.

Li, Y., Jourdain, N.C., Taschetto, A.S., Gupta, A.S., Argüeso, D., Masson, S., Cai, W., 2017. Resolution dependence of the simulated precipitation and diurnal cycle over the Maritime Continent. Clim. Dynam. 48, 4009–4028. https://doi.org/10.1007/s00382-016-3317-y.

Li, Y., Gupta, A.S., Taschetto, A.S., Jourdain, N.C., Di Luca, A., Done, J.M., Luo, J.-J., 2020. Assessing the role of the ocean–atmosphere coupling frequency in the western Maritime Continent rainfall. Clim. Dynam. 54, 4935–4952. https://doi.org/10.1007/s00382-020-05266-7.

Ling, J., Zhang, C., Joyce, R., Xie, P., Chen, G., 2019. Possible role of the diurnal cycle in land convection in the barrier effect on the MJO by the Maritime continent. Geophys. Res. Lett. 46, 3001–3011. https://doi.org/10.1029/2019GL081962.

Love, B.S., Matthews, A.J., Lister, G.M.S., 2011. The diurnal cycle of precipitation over the Maritime Continent in a high-resolution atmospheric model. Q. J. R. Meteorol. Soc. 137, 934–947. https://doi.org/10.1002/qj.809.

Madden, R.A., Julian, P.R., 1971. Detection of a 40–50 Day oscillation in the zonal wind in the tropical pacific. J. Atmos. Sci. 28, 702–708. https://doi.org/10.1175/1520-0469(1971)028<0702:DOADOI>2.0.CO;2.

Madden, R.A., Julian, P.R., 1994. Observations of the 40–50-day tropical oscillation—a Review. Mon. Weather Rev. 122, 814–837. https://doi.org/10.1175/1520-0493(1994)122<0814:OOTDTO>2.0.CO;2.

McBride, J.L., Haylock, M.R., Nicholls, N., 2003. Relationships between the Maritime continent heat source and the el niño–southern oscillation phenomenon. J. Clim. 16, 2905–2914. https://doi.org/10.1175/1520-0442(2003)016<2905:RBTMCH>2.0.CO;2.

Mellor, G.L., Yamada, T., 1982. Development of a turbulence closure model for geophysical fluid problems. Rev. Geophys. 20, 851–875. https://doi.org/10.1029/RG020i004p00851.

Metzger, E.J., Coauthors, 2014. US navy operational global ocean and arctic ice prediction systems. oceanog 27, 32–43. https://doi.org/10.5670/oceanog.2014.66.

Mlawer, E.J., Taubman, S.J., Brown, P.D., Iacono, M.J., Clough, S.A., 1997. Radiative transfer for inhomogeneous atmospheres: RRTM, a validated correlated-k model for the longwave. J. Geophys. Res. Atmos. 102, 16663–16682. https://doi.org/10.1029/97JD00237.

Mori, S., Coauthors, 2004. Diurnal land–sea rainfall peak migration over sumatera island, Indonesian Maritime continent, observed by TRMM satellite and intensive rawinsonde soundings. Mon. Weather Rev. 132, 2021–2039. https://doi.org/10.1175/1520-0493(2004)132<2021:DLRPMO>2.0.CO;2.

Nagai, T., Hibiya, T., 2015. Internal tides and associated vertical mixing in the Indonesian Archipelago. J. Geophys. Res.: Oceans 120, 3373–3390. https://doi.org/10.1002/2014JC010592.

Nagai, T., Bouruet-Aubertot, P., 2017. Nonhydrostatic simulations of tide-induced mixing in the halmahera sea: a possible role in the transformation of the Indonesian throughflow waters. J. Geophys. Res.: Oceans 122, 8933–8943. https://doi.org/10.1002/2017JC013381.

Nagai, T., Hibiya, T., 2020. Combined effects of tidal mixing in narrow straits and the ekman transport on the sea surface temperature cooling in the southern Indonesian seas. J. Geophys. Res.: Oceans 125, e2020JC016314. https://doi.org/10.1029/2020JC016314.

Nagai, T., Hibiya, T., Syamsudin, F., 2021. Direct estimates of turbulent mixing in the Indonesian archipelago and its role in the transformation of the Indonesian throughflow waters. Geophys. Res. Lett. 48, e2020GL091731 https://doi.org/10.1029/2020GL091731.

Neale, R., Slingo, J., 2003. The Maritime continent and its role in the global climate: a GCM study. J. Clim. 16, 834–848. https://doi.org/10.1175/1520-0442(2003)016<0834:TMCAIR>2.0.CO;2.

Nugroho, D., Koch-Larrouy, A., Gaspar, P., Lyard, F., Reffray, G., Tranchant, B., 2018. Modelling explicit tides in the Indonesian seas: an important process for surface sea water properties. Mar. Pollut. Bull. 131, 7–18. https://doi.org/10.1016/j.marpolbul.2017.06.033.

Osborn, T.R., 1980. Estimates of the local rate of vertical diffusion from dissipation measurements. J. Phys. Oceanogr. 10, 83–89. https://doi.org/10.1175/1520-0485(1980)010<0083:EOTLRO>2.0.CO;2.

Peatman, S.C., Matthews, A.J., Stevens, D.P., 2014. Propagation of the Madden–Julian oscillation through the Maritime continent and scale interaction with the diurnal cycle of precipitation. Q. J. R. Meteorol. Soc. 140, 814–825. https://doi.org/10.1002/qj.2161.

Peatman, S.C., Matthews, A.J., Stevens, D.P., 2015. Propagation of the Madden–Julian Oscillation and scale interaction with the diurnal cycle in a high-resolution GCM. Clim. Dyn. 45, 2901–2918. https://doi.org/10.1007/s00382-015-2513-5.

Pei, S., Shinoda, T., Steffen, J., Seo, H., 2021. Substantial Sea surface temperature cooling in the Banda Sea associated with the Madden-Julian oscillation in the boreal winter of 2015. J. Geophys. Res.: Oceans 126, e2021JC017226. https://doi.org/10.1029/2021JC017226.

Qian, J.-H., 2008. Why precipitation is mostly concentrated over islands in the Maritime continent. J. Atmos. Sci. 65, 1428–1441. https://doi.org/10.1175/2007JAS2422.1.

Ramage, C.S., 1968. Role of a tropical "maritime continent" in the atmospheric circulation. Mon. Weather Rev. 96, 365–370. https://doi.org/10.1175/1520-0493(1968)096<0365:ROATMC>2.0.CO;2.

Ray, R.D., Susanto, R.D., 2016. Tidal mixing signatures in the Indonesian seas from high-resolution sea surface temperature data. Geophys. Res. Lett. 43, 8115–8123. https://doi.org/10.1002/2016GL069485.

Ray, R. D., G. D. Egbert, and S. Y. Erofeeva, 2005: A Brief Overview of Tides in the Indonesian Seas.

Raymond, D.J., 2001. A New model of the Madden–Julian oscillation. J. Atmos. Sci. 58, 2807–2819. https://doi.org/10.1175/1520-0469(2001)058<2807:ANMOTM>2.0.CO;2.

Reynolds, R.W., Smith, T.M., Liu, C., Chelton, D.B., Casey, K.S., Schlax, M.G., 2007. Daily high-resolution-blended analyses for sea surface temperature. J. Clim. 20, 5473–5496. https://doi.org/10.1175/2007JCLI1824.1.

Robertson, R., Ffield, A., 2005. M 2 baroclinic tides in the Indonesian seas. Oceanography 18. https://doi.org/10.5670/oceanog.2005.06.

Robertson, R., Ffield, A., 2008. Baroclinic tides in the Indonesian seas: tidal fields and comparisons to observations. J. Geophys. Res.: Oceans 113. https://doi.org/10.1029/2007JC004677.

Sakaeda, N., Kiladis, G., Dias, J., 2017. The diurnal cycle of tropical cloudiness and rainfall associated with the Madden–Julian oscillation. J. Clim. 30, 3999–4020. https://doi.org/10.1175/JCLI-D-16-0788.1.

Sauvage, C., Seo, H., Clayson, C.A., Edson, J.B., 2023. Improving Wave-Based Air-Sea Momentum Flux Parameterization in Mixed Seas. J. Geophy. Res. Oceans 128, e2022JC019277. https://doi.org/10.1029/2022JC019277.

Schiemann, R., Demory, M.-E., Mizielinski, M.S., Roberts, M.J., Shaffrey, L.C., Strachan, J., Vidale, P.L., 2014. The sensitivity of the tropical circulation and Maritime Continent precipitation to climate model resolution. Clim. Dynam. 42, 2455–2468. https://doi.org/10.1007/s00382-013-1997-0.

Schiller, A., 2004. Effects of explicit tidal forcing in an OGCM on the water-mass structure and circulation in the Indonesian throughflow region. Ocean Model. 6, 31–49. https://doi.org/10.1016/S1463-5003(02)00057-4.

Seo, H., 2017. Distinct influence of air–sea interactions Mediated by mesoscale sea surface temperature and surface current in the arabian sea. J. Clim. 30, 8061–8080. https://doi.org/10.1175/JCLI-D-16-0834.1.

Seo, H., Miller, A.J., Roads, J.O., 2007. The Scripps Coupled Ocean–atmosphere regional (SCOAR) model, with applications in the eastern pacific sector. J. Clim. 20, 381–402. https://doi.org/10.1175/JCLI4016.1.

Seo, H., Subramanian, A.C., Miller, A.J., Cavanaugh, N.R., 2014. Coupled impacts of the diurnal cycle of sea surface temperature on the Madden–Julian oscillation. J. Clim. 27, 8422–8443. https://doi.org/10.1175/JCLI-D-14-00141.1.

Seo, H., Miller, A.J., Norris, J.R., 2016. Eddy–wind interaction in the California current system: Dynamics and impacts. J. Phys. Oceanogr. 46, 439–459. https://doi.org/10.1175/JPO-D-15-0086.1.

Seo, H., Subramanian, A.C., Song, H., Chowdary, J.S., 2019. Coupled effects of ocean current on wind stress in the Bay of Bengal: eddy energetics and upper ocean stratification. Deep Sea Res. Part II Top. Stud. Oceanogr. 168, 104617 https://doi.org/10.1016/j.dsr2.2019.07.005.

Seo, H., Song, H., O'Neill, L.W., Mazloff, M.R., Cornuelle, B.D., 2021. Impacts of ocean currents on the south Indian ocean extratropical storm track through the relative wind effect. J. Clim. 34, 9093–9113. https://doi.org/10.1175/JCLI-D-21-0142.1.

Shchepetkin, A.F., McWilliams, J.C., 2005. The regional oceanic modeling system (ROMS): a split-explicit, free-surface, topography-following-coordinate oceanic model. Ocean Model. 9, 347–404. https://doi.org/10.1016/j.ocemod.2004.08.002.

Shinoda, T., 2005. Impact of the diurnal cycle of solar radiation on intraseasonal SST variability in the western equatorial pacific. J. Clim. 18, 2628–2636. https://doi.org/10.1175/JCLI3432.1.

Shinoda, T., Hendon, H.H., 1998. Mixed layer modeling of intraseasonal variability in the tropical western pacific and Indian oceans. J. Clim. 11, 2668–2685. https://doi.org/10.1175/1520-0442(1998)011<2668:MLMOIV>2.0.CO;2.

Shinoda, T., Pei, S., Wang, W., Fu, J.X., Lien, R.-C., Seo, H., Soloviev, A., 2021. Climate process team: improvement of ocean component of NOAA climate forecast system relevant to Madden-Julian oscillation simulations. J. Adv. Model. Earth Syst. 13, e2021MS002658 https://doi.org/10.1029/2021MS002658.

Skamarock, W.C., Klemp, J.B., Dudhia, J., Gill, D.O., Barker, D.M., Wang, W., Powers, J. G., 2008. A Description of the Advanced Research WRF Version 3. NCAR Technical note -475+STR.

Sobel, A., Maloney, E., 2012. An idealized semi-empirical framework for modeling the Madden–Julian oscillation. J. Atmos. Sci. 69, 1691–1705. https://doi.org/10.1175/JAS-D-11-0118.1.

Sobel, A.H., Maloney, E.D., Bellon, G., Frierson, D.M., 2010. Surface fluxes and tropical intraseasonal variability: a reassessment. J. Adv. Model. Earth Syst. 2 https://doi.org/10.3894/JAMES.2010.2.2.

Sprintall, J., Gordon, A.L., Koch-Larrouy, A., Lee, T., Potemra, J.T., Pujiana, K., Wijffels, S.E., 2014. The Indonesian seas and their role in the coupled ocean–climate system. Nat. Geosci. 7, 487–492. https://doi.org/10.1038/ngeo2188.

Stoica, P., Moses, R.L., 2005. Spectral Analysis of Signals. Pearson/Prentice Hall, p. 452.

Suarez, M.J., 1999. Technical Report Series on Global Modeling and Data Assimilation, vol. 15, p. 51.

Susanto, R.D., Gordon, A.L., Sprintall, J., Herunadi, B., 2000. Intraseasonal variability and tides in Makassar strait. Geophys. Res. Lett. 27, 1499–1502. https://doi.org/10.1029/2000GL011414.

Tan, H., Ray, P., Barrett, B., Dudhia, J., Moncrieff, M.W., 2021. Systematic patterns in land precipitation due to convection in neighboring islands in the Maritime continent during MJO propagation. J. Geophys. Res. Atmos. 126, e2020JD033465 https://doi.org/10.1029/2020JD033465.

Tan, H., Ray, P., Moncrieff, M., Zhang, L., Zermeno-Diaz, D., 2022. Understanding the role of topography on the diurnal cycle of precipitation in the Maritime Continent during MJO propagation. Clim. Dynam. https://doi.org/10.1007/s00382-021-06085-0.

Vialard, J., Drushka, K., Bellenger, H., Lengaigne, M., Pous, S., Duvel, J.P., 2013. Understanding Madden-Julian-induced sea surface temperature variations in the north western Australian basin. Clim. Dynam. 41, 3203–3218. https://doi.org/10.1007/s00382-012-1541-7.

Vincent, C.L., Lane, T.P., 2016. Evolution of the diurnal precipitation cycle with the passage of a Madden–Julian oscillation event through the Maritime continent. Mon. Weather Rev. 144, 1983–2005. https://doi.org/10.1175/MWR-D-15-0326.1.

Vincent, C.L., Lane, T.P., 2017. A 10-year austral summer climatology of observed and modeled intraseasonal, mesoscale, and diurnal variations over the Maritime continent. J. Clim. 30, 3807–3828. https://doi.org/10.1175/JCLI-D-16-0688.1.

Wang, B., Liu, F., Chen, G., 2016. A trio-interaction theory for Madden–Julian oscillation. Geoscience Letters 3, 34. https://doi.org/10.1186/s40562-016-0066-z.

Wang, S., Sobel, A.H., 2017. Factors controlling rain on small tropical islands: diurnal cycle, large-scale wind speed, and topography. J. Atmos. Sci. 74, 3515–3532. https://doi.org/10.1175/JAS-D-16-0344.1.

Wang, S., Zhang, F., Sun, Y.Q., Yue, Y., Zhou, L., 2015. Regional simulation of the october and november MJO events observed during the CINDY/DYNAMO field campaign at gray zone resolution. J. Clim. 28, 2097–2119. https://doi.org/10.1175/JCLI-D-14-00294.1.

Wang, S., Tippett, M.K., Vitart, F., 2019. Prediction and predictability of tropical intraseasonal convection: seasonal dependence and the Maritime Continent prediction barrier. Clim. Dynam. 52, 6015–6031. https://doi.org/10.1007/s00382-018-4492-9.

Wei, Y., Pu, Z., Zhang, C., 2020. Diurnal cycle of precipitation over the Maritime continent under modulation of MJO: perspectives from cloud-permitting scale simulations. J. Geophys. Res. Atmos 125 https://doi.org/10.1029/2020JD032529 e2020JD032529.

Wenegrat, J.O., McPhaden, M.J., 2015. Dynamics of the surface layer diurnal cycle in the equatorial Atlantic Ocean (0°, 23°W). J. Geophys. Res.: Oceans 120, 563–581. https://doi.org/10.1002/2014JC010504.

Wheeler, M.C., Hendon, H.H., 2004. An all-season real-time multivariate MJO index: development of an index for Monitoring and prediction. Mon. Weather Rev. 132, 1917–1932. https://doi.org/10.1175/1520-0493(2004)132<1917:AARMMI>2.0.CO;2.

Yoneyama, K., Zhang, C., 2020. Years of the Maritime continent. Geophys. Res. Lett. 47, e2020GL087182 https://doi.org/10.1029/2020GL087182.

Zhang, C., Ling, J., 2017. Barrier effect of the indo-pacific Maritime continent on the MJO: perspectives from tracking MJO precipitation. J. Clim. 30, 3439–3459. https://doi.org/10.1175/JCLI-D-16-0614.1.

Zhang, C., Adames, Á.F., Khouider, B., Wang, B., Yang, D., 2020. Four theories of the Madden-Julian oscillation. Rev. Geophys. 58, e2019RG000685 https://doi.org/10.1029/2019RG000685.

Xie, Pingping, Joyce, Robert, Wu, Shaorong, Yoo, S.-H., Yarosh, Yelena, Sun, Fengying, Lin, Roger, NOAA CDR Program, 2019. NOAA Climate Data Record (CDR) of CPC Morphing Technique (CMORPH) High Resolution Global Precipitation Estimates, Version 1 [indicate subset]. NOAA National Centers for Environmental Information. https://doi.org/10.25921/w9va-q159.